Electronic Theses and Dissertations   Retrospective theses

2008

Synthesis and electrochemical study of PtIr nanomaterials

Holt-Hindle, Peter

Synthesis and Electrochemical Study of PtIr Nanomaterials

A Thesis

Presented to

The Faculty of Graduate Studies

Lakehead University

By

Peter Holt-Hindle

In partial fulfillment of the requirements

For the degree of

Masters of Science

November 2008

Canada

Abstract

Nanomaterials have a number of unique chemical and physical properties and have attracted tremendous attention due to their potential for applications in a variety of areas including fuel cell and biosensor development. The focus of this work was the design of novel platinum iridium electrocatalysts with high electrocatalytic activity towards the key electrochemical processes in direct methanol fuel cells (DMFC) and glucose sensors.

Nanoporous PtIr electrodes with different ratios of Pt to Ir were prepared on Ti and carbon nanotube (CNT) substrates using a one-step facile hydrothermal method. The nanostructure and morphology of the fabricated electrocatalysts were characterized using scanning electron microscopy (SEM), energy dispersive x-ray spectrometry (EDS), x-ray diffraction (XRD) and x-ray photoelectron spectroscopy (XPS). Electrochemical analyses were performed using cyclic voltammetry (CV), chronoamperometry (CA), linear voltammetry (LV) and electrochemical impedance spectroscopy (EIS).

Four nanoporous PtIr electrodes were synthesized in this study for comparison, $Pt_{85}Ir_{15}$, $Pt_{72}Ir_{28}$, $Pt_{60}Ir_{40}$ and $Pt_{50}Ir_{50}$. Surface analyses performed by SEM and EDS revealed that the morphology and composition of the PtIr electrocatalysts can be tuned by changing the synthesis conditions. XRD patterns show that the electrocatalysts have a face-centered cubic crystal structure and that Pt and Ir are either partially or fully alloyed. XPS spectra revealed a shift in the Pt $4f_{7/2}$ and Ir $4f_{7/2}$ binding peaks, indicating the presence of an electronic reaction between Pt and Ir. The hydrogen adsorption/desorption experiments indicated that the synthesized nanoporous PtIr electrodes possess extraordinarily high active surface area. Carbon monoxide oxidation, methanol oxidation and oxygen reduction were used as a probes to investigate the electrocatalytic activity of the nanoporous PtIr electrodes. The steady-state current density of the

nanoporous $Pt_{60}Ir_{40}$ electrode for methanol oxidation at +600 mV is over four times higher than that of the nanoporous Pt electrode, and the mass-transfer limited current of the nanoporous $Pt_{60}Ir_{40}$ electrode for oxygen reduction is about four times larger than that of the nanoporous Pt electrode.

The PtIr nanomaterial electrodes were evaluated as to their potential as non-enzymatic electrocatalysts in glucose sensors. The electrochemical measurements were conducted in a 0.1 M phosphate buffer solution at pH 7.4 with 0.15 M NaCl. Amperometric studies of the PtIr electrodes showed that the electrodes gave strong and sensitive current response to glucose concentrations ranging from 1-20 mM. The $Pt_{62}Ir_{38}$ exhibited superior sensitivity (93.7 $\mu A\ cm^{-2}$ mM^{-1}) for glucose detection and tolerance towards the presence of common interfering species.

The enhancement of the electrocatalytic activity of platinum-ruthenium electrodes towards methanol oxidation by iridium was studied by CV, CA and EIS. The electrochemical experiments showed that the inclusion of a small amount of iridium in the PtRu electrode resulted in higher electrocatalytic activity towards methanol and CO oxidation.

Acknowledgements

I would like to thank my supervisor, Dr. Aicheng Chen, for his guidance and patience while pursuing my M. Sc. degree. I would also like to thank my committee members, Dr. Stephen Kinrade and Dr. Manit Rappon, for their feedback on my thesis.

Lab members, former and current, I would like to acknowledge include Brad Miller and Kallum Koczkur for their help in getting me started in the Chen lab. I would also like to thank Samantha Nigro, Matt Amussen, Jingpeng Wang, Dr. Xinsheng Peng, Dr. Qingfeng Yi, Dr. Min Tian, and Dr. Guosheng Wu for insightful discussions.

A special thank you goes to Ed Drotar for his help in the Science Workshop and Al MacKenzie and Keith Pringnitz for their assistance in the Lakehead University Instrumentation Lab.

Finally I would like to thank my family, friends and God for their persistence, guidance and support.

Table of Contents

List of Symbols and Abbreviations

A	Ampere
AA	L-ascorbic acid
AP	4-acetamidophenol
CA	Chronoamperometry
CNT	Carbon nanotube
CO	Carbon monoxide
CP	Chronopotentiometry
CPE	Constant phase element
CV	Cyclic voltammetry
DMFC	Direct methanol fuel cell
E	Potential
EDS	Energy dispersive x-ray spectrometry
EIS	Electrochemical impedance spectroscopy
GOx	Glucose oxidase
j	Current density
LV	Linear voltammetry
Mag	Magnification
MOR	Methanol oxidation reaction
NP	Nanoporous
ORR	Oxygen reduction reaction
PBS	Phosphate buffer solution
R_{ct}	Charge transfer resistance

R_f	Resistance of the oxide film
SEM	Scanning electron microscopy
T	Temperature
UA	Uric acid
V	Voltage/potential
V vs Ag/AgCl	Voltage vs silver/silver chloride electrode
V vs SCE	Voltage vs saturated calomel electrode
XRD	X-ray diffraction
XPS	X-ray photoelectron spectroscopy
Zr	Real impedance
Zi	Imaginary impedance

Chapter 1

1. Introduction

Nanotechnology involves the fabrication and application of materials with structural features in between those of atoms and bulk materials. The building blocks of nanotechnology are nanomaterials, materials possessing at least one dimension smaller than 100 nanometers (nm). There are several different classes of nanostructured materials such as zero-dimensional (0D) nanoparticles and quantum dots, one-dimensional (1D) nanotubes and nanowires, two-dimensional (2D) thin films, and three-dimensional (3D) nanoporous materials [1]. In addition, nanostructured materials can be grouped into three categories, nanoparticles, nano-intermediates, and nanocomposites. Nanostructured materials can be fabricated by either chemical or physical processes. In the former case, a material is evaporated and then rapidly condensed to form nano-sized clusters. The products have very low contamination levels and the cluster size can be manipulated by varying the temperature, gas composition and gas flow rate. Laser ablation and chemical vapour deposition are examples of the vapour condensation route which can be used to form carbon nanotubes (CNTs). The chemical synthesis route is used to form large quantities of nano-sized agglomerates economically. It allows greater control of stoichiometry, particle size and monodispersity, although the precursor reagents may leave a contaminating residue on the produced nanomaterials. The sol-gel process, thermal decomposition and hydrothermal method are examples of chemical synthesis [2]. It is vital to control the fabrication parameters used in the synthesis of the nanomaterials as they have a direct effect on the properties of the formed nanomaterials.

Nanomaterials have a heterogeneous microstructure as their composition is made of

nanometer-sized building blocks such as nanocrystallites and the regions between the building blocks are called grain boundaries. The heterogeneous structure of nanomaterials is composed mainly of grain boundaries, which distinguishes their properties from other materials such as bulk metals, glasses and gels that are microstructurally homogeneous [3]. For example, copper nanoparticles do not exhibit the same malleability and ductility as bulk copper metal [4].

Nanomaterials have special physical properties such as high surface to volume ratios and chemical properties like electrocatalytic activity [2]. The unique properties of nanomaterials have attracted tremendous attention from researchers in industry and academia due to their potential for applications in a wide variety of areas including automobiles, bioengineering, molecular electronics, renewable energy, sensors, and wastewater purification [5]. Nanostructure materials have been employed in direct methanol fuel cells (DMFC) as electrocatalysts and electrode supporting materials to increase efficiency and reduce the consumption of precious metals [6]. Nanomaterials have also been utilized as electrode supporting materials in enzymatic biosensors and as catalysts in non-enzymatic biosensors for glucose detection, to improve stability, sensitivity and selectivity [1].

1.1 Direct Methanol Fuel Cells

Rising energy demands, depletion of fossil fuel reserves and environmental pollution have fuelled the search for energy conversion devices with high efficiency and low emissions [7]. Hydrogen or methanol powered fuel cells may have the potential to meet these requirements. While many different designs for fuel cells have been proposed and tested, the design of electrocatalysts for DMFCs was chosen as the focus of this project over that of

2

other fuel cells such as the proton exchange membrane fuel cell (PEMFC). DMFCs consume methanol whereas PEMFCs utilize hydrogen. The application of PEMFCs has been hindered due to the problem of designing a safe, reliable and economical hydrogen storage and distribution system. Conversely methanol has high energy density on the same magnitude of hydrogen, is much safer and simpler to store and distribute and is consumed in DMFCs at ambient temperature. It is important to recognize that DMFCs are very complex systems and face a number of challenges to overcome before they would be ready for commercialization. Many of these challenges are fundamental problems such as the methanol crossover, the management of heat, relatively low power density and the management of water [8].

1.2 Methanol Oxidation Reaction

The two key reactions in a fuel cell are the methanol oxidation reaction (MOR) at the anode and the oxygen reduction reaction (ORR) at the cathode. The chemical equations for the reactions are:

Anode: $CH_3OH + H_2O \rightarrow CO_2 + 6H^+ + 6e^-$

Cathode: $\underline{(3/2)O_2 + 6H^+ + 6e^- \rightarrow 3H_2O}$

Net reaction: $CH_3OH + (3/2)O_2 \rightarrow CO_2 + 2H_2O$

There are a number of factors influencing the material development of electrocatalysts for DMFCs including cost effectiveness, desirable electrical conductivity, high electrocatalytic activity and long-term stability [9]. Of the pure metals the most promising candidate for application in DMFCs is platinum. While the mechanism for methanol oxidation on Pt has been extensively researched, some details of it are not completely understood. The proposed mechanism for the oxidation of methanol on platinum electrodes is described below [7]:

Step 1: $CH_3OH \rightarrow (CH_3OH)_{ads}$ (Methanol adsorption)

3

Step 2: $(CH_3OH)_{ads} \rightarrow (CO)_{ads} + 4H^+ + 4e^-$ (C-H bond activation)

Step 3: $H_2O \rightarrow (H_2O)_{ads}$ (Water adsorption)

Step 4: $(H_2O)_{ads} \rightarrow (OH)_{ads} + H^+ + e^-$ (Water activation)

Step 5: $(CO)_{ads} + (OH)_{ads} \rightarrow CO_2 + H^+ + e^-$ (CO oxidation)
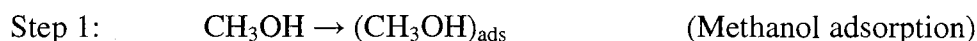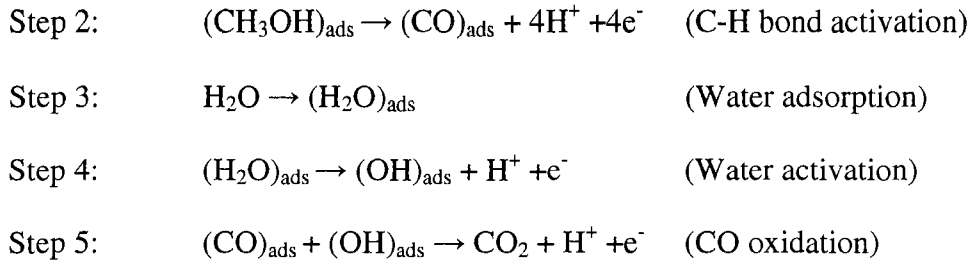
One of the major challenges hindering the commercialization of DMFCs is the slow methanol oxidation kinetics, which is caused by two of the five steps in the methanol oxidation reaction, methanol adsorption and CO oxidation. As shown in Figure 1.1, three adjacent Pt sites are needed initially for the adsorption of methanol.
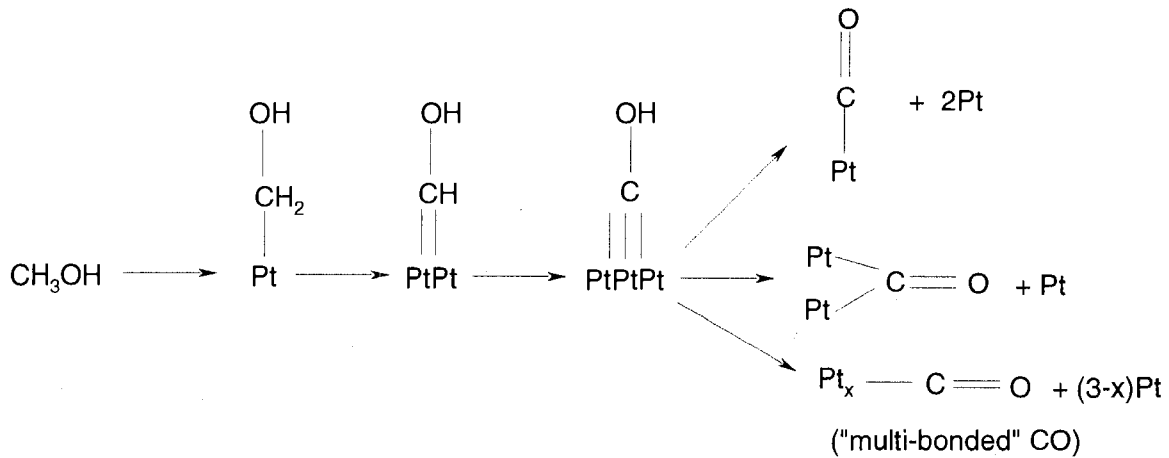
Figure 1.1: Scheme of the adsorption of methanol to the surface of a Pt electrode [10]. Two of these sites become unoccupied during the subsequent reaction steps that yields the linear bonded –CO or bridge bonded –CO species, however, the liberated Pt sites do not possess the C_{3v} symmetry needed for another methanol molecule to adsorb. Overall a flow of four electrons occurs for each adsorbed –CO species, which has two implications. First being that a net charge of more than one electron per Pt site exists for a Pt surface highly covered with CO, although no connection has been drawn between the net flow of charge and the dominating adsorbate species. Secondly, the adsorption of methanol could follow a self-feeding mechanism through surface diffusion processes in the inter-adsorbate conversion

4

processes. The methanol adsorption process is very complex and new experimental techniques are required to determine the reaction kinetics as well as details of the dissociation and diffusion steps involved [10]. The use of high surface area nanomaterials as electrocatalysts and electrode supporting materials aids in improving the kinetics of methanol adsorption. Peng et al. fabricated nanoporous platinum networks with a two-step seed-assisted hydrothermal deposition technique and found that the electrocatalysts had an electroactive surface area over 20 times higher than a Pt wire and a much higher current density during the electrochemical oxidation of methanol [11]. Chen et al. used a hydrothermal method to disperse platinum nanoparticles onto multiwalled CNTs. Their electrochemical testing revealed that the synthesis conditions affected the size and the activity of the platinum nanoparticles and, overall, the electrocatalysts had high electrocatalytic activity towards the oxidation of methanol [12].

While the main product from the oxidation of methanol on a Pt electrode is CO_2, significant amounts of CO, formaldehyde, formic acid, and methyl formate are formed. Due to the number of different products formed, most studies conclude that there are multiple mechanisms for the reaction [13]. The formation of CO is the most significant as it can occupy the active catalytic sites on the Pt electrode, slowing the reaction kinetics. As described above in Figure 1.1, CO is removed from the surface of the Pt electrode in an oxidative step involving OH species that are formed through the activation of water. With a pure Pt electrode this water activation step requires high potentials, which is undesirable for the application of Pt electrodes as anodes in DMFCs. To date, incorporating Ru into Pt catalysts has yielded the best results for enhancing the electrocatalytic properties of the Pt electrodes towards the oxidation of methanol. Two mechanisms have been proposed to

account for this affect. The first mechanism is a ligand effect whereby the electronic

properties of Pt are modified by the Pt-Ru orbital overlap, which weakens the strength of the

bond between Pt and CO. The other is a bi-functional mechanism whereby

oxygen-containing species are adsorbed on Ru atoms which promotes the oxidation of CO to

CO_2 on neighbouring Pt sites, as summarized below [14]:

Step 1: $\quad Pt + CH_3OH \rightarrow Pt(CO)_{ads} + 4H^+ + 4e^-$ $\qquad$ (CO adsorption)

Step 2: $\quad Ru + H_2O \rightarrow Ru(OH)_{ads} + H^+ + e^-$ $\qquad$ (OH adsorption)

Step 3: $\quad Pt(CO)_{ads} + Ru(OH)_{ads} \rightarrow CO_2 + Pt + Ru + H^+ + e^-$ $\quad$ (CO oxidation)
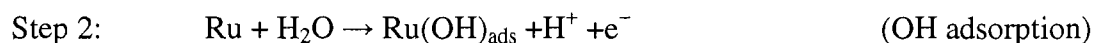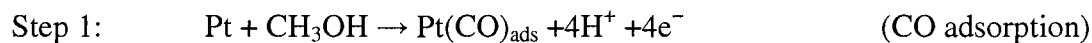
In addition to Ru, a variety of metals have been investigated to determine their capabilities to

generate oxygenated species at lower potentials. Efforts to improve the performance of the

anode in DMFCs have focused on coupling these metals with platinum to fabricate various

Pt-based bimetallic alloys, nanoparticle mixtures and composites, including Au [15], Co [14],

Ni [14,16], Ru [7-20], Mo [21], W [22,23], Ir [24] and Sn [25-27]. These investigations have

demonstrated that the Pt-based bimetallic electrodes have enhanced electrocatalytic activity

over bulk platinum electrodes. Given the bi-functional mechanism whereby Ru enhances the

electrocatalytic activity of platinum, the fabrication of anodes with Pt and oxygen evolution

catalysts such as iridium oxide may enhance their electrocatalytic activity towards methanol

electro-oxidation. Hefny and Abdel-Wanees found that iridium oxide coatings produced an

anodic current in the presence of methanol, which was attributed to the oxidation of methanol

via electrochemically generated oxygen species as described in Figure 1.2 [28].

6

$$\text{Ir}\!=\!\!O + H\!-\!\!\overset{\displaystyle H}{\underset{\displaystyle H}{\overset{|}{\underset{|}{C}}}}\!-\!OH \longrightarrow \text{Ir}\!-\!O\!-\!H\!-\!C\overset{H}{\underset{H}{\diagdown}}OH$$
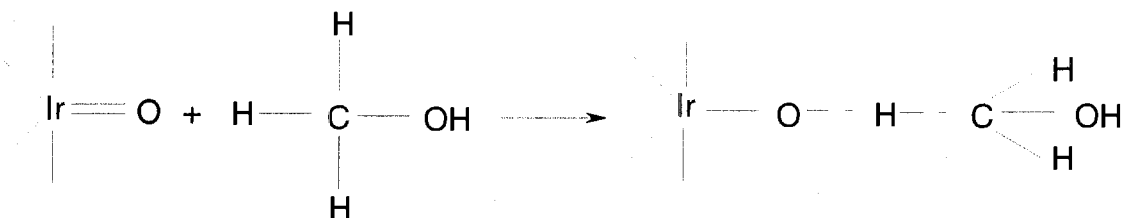
Figure 1.2: Generation of oxygenous species on iridium oxide electrodes [28].

DMFCs also require an acidic medium to prevent the formation of carbonates, which can fill up the pores of the membrane of the catalytic layer. Iridium oxide is stable in the pH and temperature ranges in which DMFCs operate; moreover, it has good electrical conductivity, and high electrocatalytic activity toward oxygen evolution [28]. These properties make iridium oxide a promising candidate for use as a co-catalyst in the development of electrocatalysts for DMFCs.

1.3 Oxygen Reduction Reaction

The ORR has been widely investigated due to the application of oxygen cathodes in DMFCs. Among the precious metals, platinum is considered to be the best electrocatalyst for the electro-reduction of oxygen. The kinetics and mechanism of the ORR have been extensively investigated on a variety of substrates and two mechanisms have been proposed: a two electron pathway and a four electron pathway. The two electron pathway takes place on gold electrodes [29], reducing oxygen gas to hydrogen peroxide [30]:

$$O_2 + 2H^+ + 2e^- \rightarrow H_2O_2; \; E^0 = 0.67 \text{ V}$$
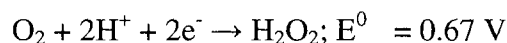
The four electron pathway occurs on platinum electrodes and reduces oxygen to water [30]:

$$O_2 + 4H^+ + 4e^- \rightarrow H_2O; \; E^0 = 1.229 \text{ V}$$
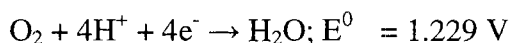
The reaction involves the fast chemical adsorption of O_2 to the Pt surface followed by the protonation of O_2 which is the rate determining step. The ORR is very complex and not yet

completely understood. The formation of inhibiting intermediates such as O_{ads}, OH_{ads} and

O_2H_{ads} indicates that multiple reaction pathways exist as proposed below in Figure 1.3.

$$O_2 + H^+ + e^- \xrightarrow{\text{K}_1} (O_2H)_{ads}$$

$$(O_2H)_{ads} + H_2O \underset{K_2}{\overset{K_2}{\rightleftharpoons}} 3(OH)_{ads}$$

$$(OH)_{ads} + H^+ + e^- \underset{}{\overset{K_3}{\rightleftharpoons}} H_2O$$
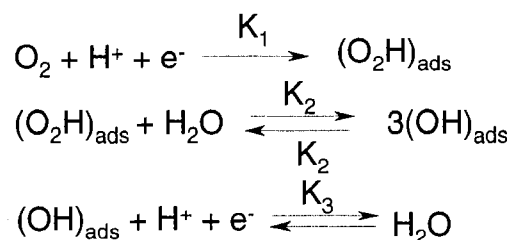
Figure 1.3: Formation of intermediates in the ORR in acid solutions [31].

The performance of Pt electrodes towards the ORR is limited at high potentials due to

the formation of these adsorbed oxygen species at high potentials. Thus, the operating

potential of the cell must be reduced from the theoretical value of 0.987 V to 0.558 V vs.

SHE where oxygen reduction occurs on the cathode. The adsorbed intermediates cause a

significant loss in the overall performance of the fuel cell, an issue that needs to be addressed

to enable the commercial application of DMFCs. Efforts to improve the electrocatalytic

performance of the cathode towards the reduction of oxygen have focused on improving the

catalytic effectiveness of platinum by either dispersing catalyst particles onto an electrode

support with a high surface area or forming alloys of platinum with other metals. For

instance, Kongkanand et al. dispersed platinum nanoparticles onto single-walled CNTs and

discovered that the resulting electrodes had high stability, a lower onset potential and an

increased electron-transfer rate constant for oxygen reduction [32]. A variety of Pt-based

bimetallic alloys have been fabricated and tested, including Pt-Co [33], Pt-Cr [34,35], Pt-Ir

[39], Pt-Ni [36], Pt-Ru[37], Pt-Ti [38] and Pt-W [39]. In summary, these studies have

demonstrated that several factors are responsible for the enhancement of the electrocatalytic

activity of Pt electrodes, including large electroactive surface area, the properties of the

electrode supporting materials and the properties of the cocatalysts.

1.4 Glucose Sensing

Diabetes is a metabolic disorder evident in blood glucose concentrations outside the normal range of 4.4-6.6 mM which results from insulin deficiency and hyperglycemia. Diabetes is one of the leading causes of disability and mortality nationally and may cause complications such as blindness, kidney failure and increased risk of heart disease [40]. Thus, there is tremendous demand for developing precise and quick methods to monitor blood glucose concentrations [41-44]. Understanding the electro-oxidation of glucose is vital for developing fast and reliable sensors with high sensitivity and high selectivity. Glucose sensors fall into two categories: enzymatic and non-enzymatic. Enzymatic glucose sensors utilize an enzyme, such as glucose oxidase (GOx), to oxidise glucose which is attached to the electrode surface by chemisorption, entrapment within a film or passive adsorption. Enzymatic glucose sensors have the advantages of high sensitivity and high selectivity towards glucose detection, as glucose oxidase has a high affinity for glucose. Many advances were made following the first enzyme electrode fabricated by Clark and Lyons [45]. The first generation sensor employed oxygen as an electron mediator between the enzyme and the electrode surface. The current response from H_2O_2 detection was proportional to the glucose concentration [46]. The second generation glucose utilized artificial mediators to overcome low oxygen concentrations by assisting with the transfer of electrons between the enzyme and the electrode [46]. The third generation of glucose sensors possesses the advances of direct electron transfer to help eliminate possible interferences. In this generation electrons are transferred from the enzyme through a series of electron relays in a self assembled monolayer to the electrode surface [47]. The direct electron transfer of the third generation sensor eliminates oxygen dependence and interference from redox-active species.

Despite all the advances from 40 years of development, enzymatic glucose sensors have a number of drawbacks which originate from the nature of the enzyme. Temperature, chemical and thermal instabilities, pH and humidity are all potentially damaging factors that can denature the enzymes and cause the loss of sensor activity [46]. The stability problems of enzymatic catalysts are overcome by using metal catalysts, such as platinum which has shown the best sensitivity towards glucose. Mechanistic studies of the electrochemical oxidation of glucose on platinum in neutral phosphate buffer indicate that glucono-δ-lactone is the product from the two-electron oxidation of glucose via the dehydrogenation at the C_1 carbon, which is hydrolyzed to form the final product gluconic acid [48]. Cyclic voltammetric experiments reveal three distinct potential regions where glucose is electrochemically oxidized on Pt surfaces. The region between -0.09 and 0.11 V vs. SCE is referred to as the hydrogen region, where glucose oxidation is associated with the adsorbed hydrogen atoms on the Pt surface [48]. The double layer region occurs between 0.16 and 0.56 V vs. SCE where only charging or discharging because of double layer capacitance occurs [49]. Finally the Pt oxide region occurs at potentials above 0.86 V versus SCE wherein glucose reacts with the Pt oxide layer on the electrode surface [45]. Further mechanistic studies are needed to better understand the electrochemical behaviour of glucose on platinum electrodes and determine the optimal potential range for the development of amperometric sensors.

While the kinetically controlled oxidation of glucose on bulk Pt surfaces is slow and results in insufficient sensitivity and selectivity, nanostructured Pt materials have shown good electrocatalytic properties towards glucose oxidation. For instance, highly ordered platinum nanotube arrays fabricated by electrochemical deposition onto a modified anodic

alumina membrane showed increased sensitivity towards glucose compared to a smooth Pt electrode [50]. Subsequent investigations have modified the Pt surface with Bi, Pb, Tl, WO_3 [51-54]. These bimetallic electrodes have shown catalytic activity towards glucose under acidic and basic conditions. The activity of Pt-based electrodes is also reduced by chloride ions (present under physiological conditions) and chemiadsorbed intermediates from glucose oxidation that block the active catalytic sites. Various endogenous species, including L-ascorbic acid (AA), 4-acetamidophenol (AP) and uric acid (UA), are oxidized in the same potential range as glucose. Although the physiological concentration of these is low (0.1 mM AA, 0.1 mM AP and 0.2 mM UA) they produce oxidation currents which are comparable to those produced by much higher glucose concentrations, due to their faster electron transfer rates. Nanoporous bimetallic PtPb electrodes fabricated by Wang et al. showed insensitivity towards AA, AP and UA under physiological conditions [55]. However, the practical application of PtPb and other bimetallic electrodes is limited due to the toxicity of heavy metal elements. Iridium and Iridium oxide are attractive candidates in biosensors due to their biocompatibility, excellent electrical conductivity and stability. Several studies have shown that glucose sensors fabricated with GOx and Ir or IrO_2 have good stability and increased the sensitivity towards glucose via the detection of hydrogen peroxide at low potentials where the response from common endogeneous species is low [56-58].

1.5 Rationale and Scope of the Thesis

This chapter has provided an overview of the fundamentals of nanotechnology, including the classes and categories of nanomaterials as well as their synthetic fabrication routes. The heterogeneous microstructure of the nanostructured materials results in unique physical, chemical and electronic properties and gives nanomaterials tremendous potential

11

for application in a wide variety of fields. This chapter has also reviewed the key reactions that take place in DMFCs and glucose sensors. The scope of this thesis is to investigate the key electrochemical reactions that take place in DMFCs and glucose sensors and will not address any of the fundamental problems associated with design of these systems. The focus will be the design of bimetallic platinum-iridium nanoporous network electrocatalysts with high electrocatalytic activity towards the MOR, ORR and glucose oxidation. A facile one-step hydrothermal synthesis method will be employed to control the metallic composition, particle deposition and particle size.

The next chapter will elaborate on the chemical vapour deposition, electrochemical deposition and, hydrothermal methods used for electrode fabrication as well as the surface analysis techniques and the electrochemical methods used to characterize the nanostructured materials. Chapter 3 will present the electrocatalytic properties of the PtIr nanostructured materials in the context of the MOR and ORR. Chapter 4 will detail the electrocatalytic properties of the PtIr nanomaterials for the non-enzymatic detection of glucose. Chapter 5 will present initial studies of the electrocatalytic activity of PtRu nanostructured materials enhanced with Ir, a summary of the results, conclusions and, possibilities for future work.

Chapter 2

Experimental Section

2. Methodology

The fabrication of Pt-based nanomaterials is accomplished through a variety of methods such as electrochemical deposition, electroless deposition, sol-gel derived processes and impregnation of metal precursors followed by chemical or physical reaction [59]. The extensive research into synthesis procedures reflects how the electrocatalytic performance of Pt-based electrocatalysts is dependent on the nature of the metal elements, surface compositions, morphology and the presence of impurities. A facile one-step hydrothermal method was used to fabricate the Pt-based nanomaterials. The hydrothermal method is reproducible, produces nanomaterials with a mixture of metallic and metal oxide species and is suitable for the synthesis of a wide range of bi-metallic and tri-metallic nanosized electrocatalysts with large active surface areas and high electrocatalytic activity. Titanium was used as a substrate for the majority of the electrodes in this study due to its good corrosion resistance and reasonable cost.

The properties of the electrode substrates can also have a pronounced effect on the electrocatalytic activity of electrocatalysts. CNTs are an attractive candidate for electrode supporting materials due to their unique chemical, mechanical and electronic properties as well as their high surface area. Like other nanomaterials, CNTs can be synthesized with a variety of methods including arc discharge, laser ablation, chemical vapour deposition and flame synthesis. These techniques are hindered from being used for large-scale production of CNTs due to complex fabrication and purification procedures, extremely high temperature conditions (2000-4000 °C), low yields and dangerous carbon sources such as acetylene [60].

Chemical vapour deposition was chosen as a synthesis method to form CNTs as it is efficient, inexpensive, safe and the synthesis conditions of growth time, temperature, catalysts and carbon source can be used to tune the morphology of the formed CNTs.

2.1 Materials

Titanium (99.2%) from Alfa Aesar was cut into 1.25 cm x 0.8 cm x 0.5 mm plates. $H_2PtCl_6\cdot6H_2O$, $RuCl_3$, $IrCl_3$, D-glucose, L-ascorbic acid, uric acid, 4-acetamidophenol, potassium phosphate dibasic, potassium phosphate monobasic, sodium chloride, cobalt sulphate, methanol (99.9%), hydrogen peroxide (30%), isopropyl alcohol (99.5%), nitric acid (68.0%), formaldehyde (37% weight in water), hydrochloric acid (37.5%), sulphuric acid (99.999%) were all used as received from Aldrich. Type-I deionized water (18.2 MΩ cm) was used for cleaning and the preparation of all solutions.

2.2 Electrode Fabrication

2.2.1 Carbon Nanotube Electrodes

A graphite rod with a diameter of 1 cm was sawed into 0.6-0.8 mm sections. The sections were sanded with standard aluminium oxide sandpaper. Both faces of the graphite rod were successively polished with 40, 180 and 400 grit sandpaper until there were no striations visible on the surface. The face in contact with the electrolyte was subsequently polished with 1500 grit sandpaper until the surface was visibly shiny. Finally, the sections were ultrasonically cleaned in a 1:1 mixture of acetone and deionized water to remove the polishing residue.

The electrochemical (EC) deposition of the cobalt catalyst was performed using a two electrode system. A titanium waffle electrode was used as the counter electrode and a

titanium rod electrode, with a Teflon® holder to seal the graphite substrate to the electrode, was used as the working and reference electrodes. The EC deposition was carried out in 1.0 M $CoSO_4$ solution with a current density of -5.0 mA for 60 seconds. The CP experiment was executed using the Voltalab 40 potentiostat PGZ301 and Voltamaster (Version 5.1) electrochemical software. Following the deposition, the samples were rinsed with type-I deionized water from before CNT synthesis.

The CNTs were synthesized in a sealed quartz flow reactor (4.5 cm x 70 cm) that was heated by a conventional horizontal tube furnace. The graphite samples with the cobalt catalyst deposited on the surface were placed on a ceramic boat in the center of the reactor tube. MKS mass flow controllers were used to regulate the flow of gas going into the reactor. The reactor was purged using pure argon gas (99.999%) at a flow rate of 200 cubic centimetres per minute for 3 hours, and then heated to 750°C at a rate of 30 °C per minute. After the temperature of 750 °C was reached, acetone was carried into the reactor tube for 1.5 hours via the argon stream which was bubbled through liquid acetone. Finally, the system was allowed to cool to room temperature while under a continuous purge of pure argon.

Following the synthesis, the CNTs were purified by successively submersing them for 1.5 hours in 3.0 M HNO_3 and a 3:1 ratio of 3.8 M H_2SO_4 and 7.5% H_2O_2.

2.2.2 Nanoporous Pt Network Electrodes

Three dimensional nanoporous Pt network electrodes were successfully fabricated. Titanium plates were etched for 20 minutes in a 17% HCl solution at 85 °C. Following the etching, the plates were rinsed with pure water. The treated titanium substrate was transferred into a Teflon® lined autoclave containing: 5.4 x 10^{-5} mol $H_2PtCl6 \cdot 6H_2O$, 0.01

mol formaldehyde and 0.0026 mol HCl, and then heated to 180 °C for 10 hours. Once the samples had cooled to room temperature, they were again washed with pure water.

2.2.3 Nanoporous PtIr Network Electrodes

Titanium plates were etched in a 17% HCl solution at 85 °C for 20 min and then rinsed with pure water. The etched titanium plates were placed into clean Teflon® autoclaves containing 5.4 x 10^{-5} mol $H_2PtCl6 \cdot 6H_2O$, 0.032 mol formaldehyde, 0.006 mol HCl and different volumes of a 0.14 M $IrCl_3$ solution at 180 °C for 10 hours. After the samples cooled to room temperature, the coated substrates were removed and rinsed with pure water.

2.2.4 Nanoporous PtRu and PtRuIr Network electrodes

Titanium plates were etched with a 17% HCl solution at 85 °C for 20 min to remove the surface oxide layer. The etched substrates were transferred into a Teflon®-lined autoclave containing 5.4 x 10^{-5} mol $H_2PtCl6 \cdot 6H_2O$, 0.01 mol formaldehyde, 3.59 x 10^{-5} mol $RuCl_3$ and 0.0026 mol HCl, and then was heated for 10 hours at 180 °C. The samples were allowed to cool to room temperature, before being rinsed with pure water. The fabrication of the PtRuIr electrode was identical to PtRu, except for the addition of 9.8 x 10^{-6} mol $IrCl_3$ in Isopropanol.

2.3 Surface Analysis

The nanostructure, morphology and elemental surface composition of the synthesized CNTs and Pt-based electrocatalysts were characterized using scanning electron microscopy (SEM) (JEOL JSM 5900LV) and energy dispersive X-ray spectrometry (EDS) (Oxford Links ISIS). X-ray diffraction (XRD) analysis was performed using a Phillips PW 1050-3710 diffracometer with Cu Kα radiation in conjunction with the database of the International

16

Centre for Diffraction Data (ICDD). X-ray photoelectron spectroscopy (XPS) (Omicron EA-125 energy analyzer and a multi-channel detector) was performed using a monochromatic Mg Kα X-ray source (hv=1253.6 eV). The water contact angle of the CNTs was determined using optical microscopy.

2.4 Electrochemical Experiments

All electrochemical experiments including CV, LV, CA, CP and EIS were performed using the classical three-electrode system. The reference electrode used was a saturated calomel electrode and was connected to the working electrode through a salt bridge filled with saturated KCl solution. The counter electrode used was a coiled platinum wire that was flame annealed prior to each electrochemical experiment. The geometric area of each working electrode was used to calculate the current density. For the Ar-saturated experiments, the solutions were bubbled with ultrapure argon gas (99.999%) at least 20 min before the electrochemical measurements, and argon continuously flowed over the surface of the electrolyte during the measurements. All measurements were conducted at ambient temperature (20 ± 2 °C).

For the fuel cell investigation, the majority of the electrochemical experiments were performed using a VoltaLab 40 potentiostat PGZ301.The exceptions were EIS experiments which were performed with a Solartron 1287 potentiostat, Solartron 1252B frequency response analyzer and ZPlot software. The amplitude of modulation potential for the EIS measurements was 10 mV, and the frequency was changed from 40 kHz to 25 mHz. For the carbon monoxide oxidation experiments, the potential was held at -0.1V for 740 s. Carbon monoxide was purged into the cell for 600 s, argon for 120 s followed by 20 s of rest. For the oxygen reduction experiments, the O_2-saturated solution was achieved by bubbling pure

oxygen gas through the 0.5 M H_2SO_4 solution for 5 min before experiments. O_2 gas was continuously bubbled through the solutions during measurements at a rate of 20 mLmin^{-1} to keep the solution O_2 saturated during the experiment and increase the mass transfer to the electrode surface. For glucose testing, the electrochemical experiments were conducted using a CHI 660B electrochemical workstation with an Ag/AgCl reference electrode. A magnetic stir bar was used as needed to agitate the solution following injections of glucose.

Chapter 3

Electrocatalytic Activity of Nanoporous Pt-Ir Materials toward Methanol Oxidation and Oxygen Reduction

3.1 Introduction

Methanol oxidation and oxygen reduction are key anodic and cathodic reactions in direct methanol fuel cells (DMFCs). Platinum electrocatalysts have shown high electrocatalytic activity towards methanol oxidation. However, one of the major drawbacks of using pure Pt electrodes is that their performance is limited by the formation of strongly adsorbed intermediate CO on the electrode surface [13]. The development of novel electrode materials with higher activity will help to increase the efficiency of the DMFC. Over the last two decades, investigation in this field has been focusing on the development of Pt-based electrocatalysts, such as Pt-based bimetallic alloys, nanoparticle mixtures and composites. A wide variety of other metals coupled with platinum to form Pt-based electrocatalysts have been synthesized and tested, including Au [15], Co [14], Ni [14,16] Ru [17-20], Mo [21], W [22,23], Ir [24,61] and Sn [25-27]. These studies have demonstrated that the Pt-based bimetallic electrodes have enhanced electrocatalytic activity over bulk platinum electrodes.

In addition to methanol oxidation, the oxygen reduction reaction (ORR) has been widely investigated due to the application of oxygen cathodes in electrochemical energy conversion systems, including fuel cells. Although investigation into the kinetics and mechanism of the ORR has confirmed that platinum is the best electrocatalyst among pure metals for the reaction, practical applications involving large amounts of platinum are hampered by its high cost. Recent efforts have focused on improving the catalytic effectiveness of platinum by dispersing the catalyst particles onto an electrode support with a high surface area and forming alloys of platinum with other metals. A variety of Pt-based

bimetallic alloys have been fabricated and tested, including Pt-Co [33], Pt-Cr [34,35], Pt-Ir [61], Pt-Ni [36], Pt-Ru [37], Pt-Ti [38] and Pt-W [39]. All these studies have shown that several factors are responsible for the enhancement of the electrocatalytic activity of Pt electrodes, including large electroactive surface area, the properties of the electrode supporting materials and the properties of the co-catalysts.

3.2 Surface Characterization of Nanoporous PtIr Networks

The surface morphology of the prepared PtIr electrodes was characterized using SEM. All the prepared PtIr electrodes possess nanoporous network structures. As evident from the images in Figure 3.1, the titanium substrate is completely covered by PtIr bimetallic particles with sizes of 50 – 500 nm. Ir^{3+} and Pt^{4+} ions were reduced simultaneously by formaldehyde under hydrothermal conditions, resulting in PtIr bimetallic particles being deposited on the titanium substrate. As the reduction continued, the bimetallic particles started forming on top of one another in a compact arrangement, yielding the nanoporous three-dimensional network structure.

The normalized atomic ratio of the Ir content was determined by quantitative EDS analysis which revealed that the compositions of the samples are: S1, $Pt_{85}Ir_{15}$; S2, $Pt_{72}Ir_{28}$; S3, $Pt_{60}Ir_{40}$; and S4, $Pt_{50}Ir_{50}$. At low energy (around 2 KeV) the spectra for the S0 and S4 electrodes are very similar, that is the platinum and iridium peaks strongly overlap. However, at high energy the peaks are easily distinguishable as shown in the inset of Figure 3.2. This trend is consistent with previous reports for platinum and iridium nanomaterials [59,66].

XRD analysis was used to characterize the phase and structure of the as-synthesized nanoporous PtIr electrodes. Figure 3.3 shows the corresponding XRD patterns for a bare titanium substrate, S0 and S4. It is evident that the S0 and S4 electrodes match the pattern
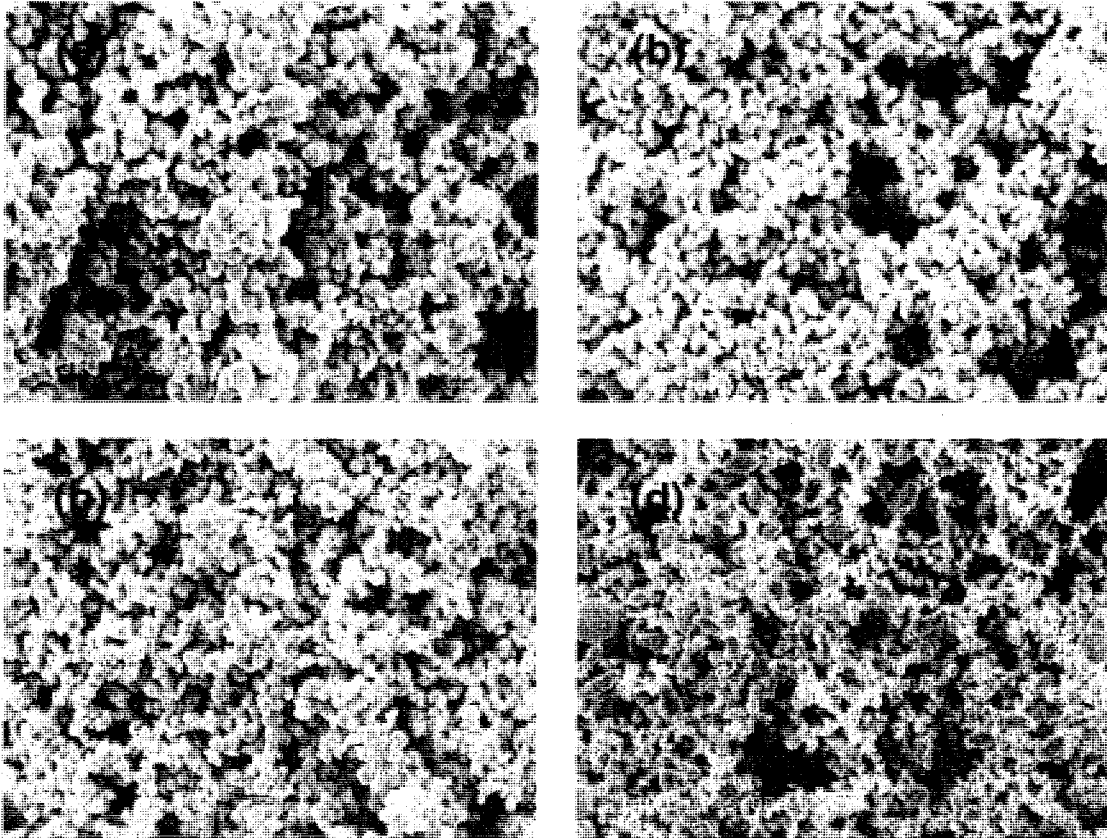
Figure 3.1. SEM images of (a) nanoporous $Pt_{85}Ir_{15}$ (S1), (b) nanoporous $Pt_{72}Ir_{28}$ (S2), (c) nanoporous $Pt_{60}Ir_{40}$ (S3) and (d) nanoporous $Pt_{50}Ir_{50}$ (S4) at 6,000x magnification.

of a hexagonal Ti crystal in the ICDD database (PDF No. 44-1294) although with lower intensities due to the Ti surface being covered by the nanoporous networks. The nanoporous Pt and PtIr electrodes both display the (111), (200) and (220) reflections, which are characteristic of the face-centred-cubic crystal structure. In comparison to nanoporous Pt, the PtIr peaks exhibit a positive shift in the 2θ values, which corresponds with decreased d-spacing values and lattice constants. Further evidence was provided by quantitative calculations of the lattice constant (a) from the observed diffraction angles of the (220) reflection peak, which revealed a values of 0.392 and 0.388 for nanoporous Pt and PtIr, respectively. The peak lines for the PtIr electrode appear between the reflections of pure Pt and pure Ir, and there are no (111), (200) or (220) reflections to indicate the presence of pure Ir in the PtIr pattern [59]. The sum of this evidence shows that the Pt and Ir are either fully or partially alloyed [39,67,68].

XPS was used to complete the characterization of the Pt-Ir electrodes. In Figure 3.4a, two 4f binding peaks of Pt identified as the $4f_{7/2}$ and $4f_{5/2}$ are evident for the nanoporous Pt and PtIr electrode. Figure 3.3a shows the $4f_{7/2}$ and $4f_{5/2}$ doublets of the nanoporous Pt occur at 71.0 and 74.3 eV, which is in agreement with previous studies [39,69]. The $4f_{7/2}$ and $4f_{5/2}$ doublets of Pt of the PtIr electrode occur at 71.4 and 74.7 eV, which shows a positive shift of 0.4 eV occurs for the $4f_{7/2}$ binding peak for PtIr. The $4f_{7/2}$ and $4f_{5/2}$ doublets of pure Ir occur at 60.9 and 63.9 eV [70], in comparison to the doublets at 60.6 and 63.6 eV for the PtIr electrode shown in Figure 3.3b. Therefore, a negative shift of 0.3 eV occurs for the Ir $4f_{7/2}$ binding peak for the PtIr electrode in comparison to pure Ir [59]. A shift in the binding energy of core-level orbitals corresponds to a change in electron density, which indicates the
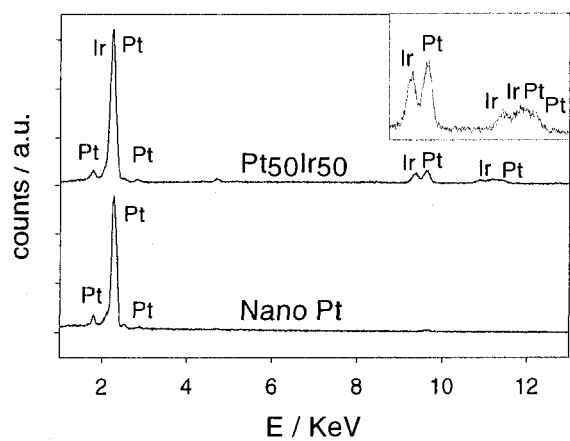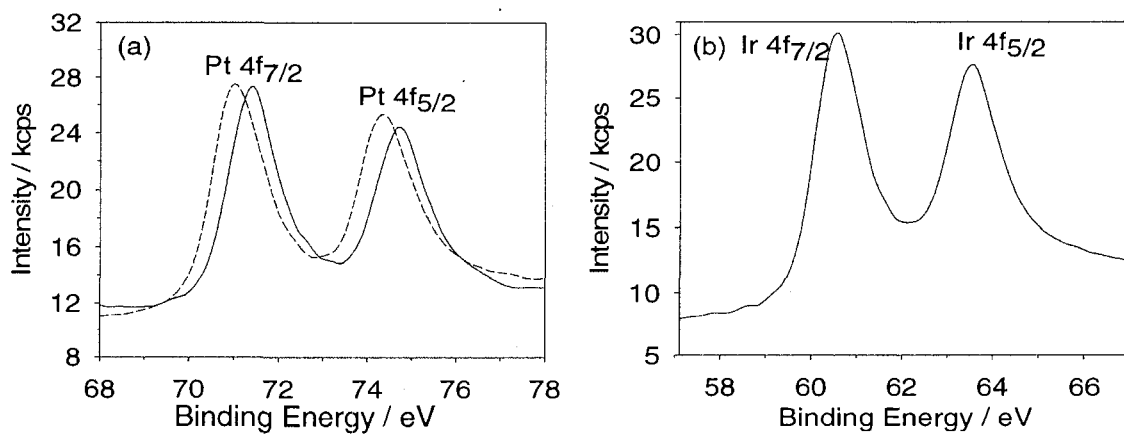
Figure 3.2. EDS spectra of nanoporous Pt (S0) and nanoporous Pt$_{50}$Ir$_{50}$ (S4).
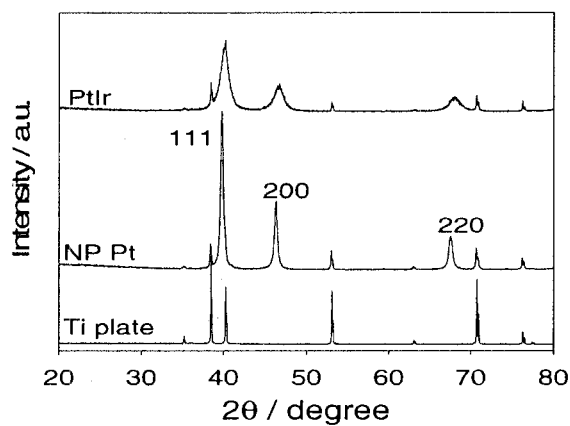
Figure 3.3. XRD patterns of the Ti plate, nanoporous Pt (S0) and nanoporous Pt$_{50}$Ir$_{50}$ (S4).


Figure 3.4. XPS spectra of the Pt 4f (a) and Ir 4f regions (b) for the nanoporous Pt (S0)

[dashed line] and nanoporous Pt$_{50}$Ir$_{50}$ (S4) [solid line].

23

presence of an electronic interaction between Pt and Ir, such as an intra-atomic charge transfer [39].

3.3 Characteristics of Hydrogen Adsorption

The cyclic voltammograms (CVs) for samples S0, S1, S2, S3 and S4 in 0.5 M H_2SO_4 at a sweep rate of 20 mV/s are shown in Figure 3.5a. As seen in Figure 3.5a, samples S0 to S3 display similar hydrogen adsorption/desorption properties: two peaks are observed on both the forward and reverse scans and their peak intensities increase with the increasing iridium content from 0% (S0) to 40% (S3). By further increasing the iridium content to 50%, the peak intensities of the hydrogen adsorption/desorption on the S4 electrode surface decrease, indicating a reduction in the number of available Pt surface sites. While the current density of the peaks for the samples varies, all four nanoporous PtIr electrodes have a much higher current density than the nanoporous Pt electrode. According to Schmidt et al. [62], the number of active sites available on the surface of a Pt electrode for hydrogen adsorption and desorption can be determined from the integrated intensity of these peaks.

Thus, the electroactive surface areas of these samples can be estimated from the hydrogen adsorption/desorption peaks. The charge for hydrogen adsorption on the nanoporous Pt electrode (S0) is 18.57 mC cm^{-2}. The charges for the hydrogen adsorption on the surface of S1, S2, S3 and S4 are 32.9, 92.2, 104.7 and 60.3 mC cm^{-2}, respectively. These indicate that the electroactive surface areas of the nanoporous PtIr electrodes are approximately 1.77, 4.96, 5.64 and 3.25 times larger than that of the nanoporous Pt electrode, respectively.
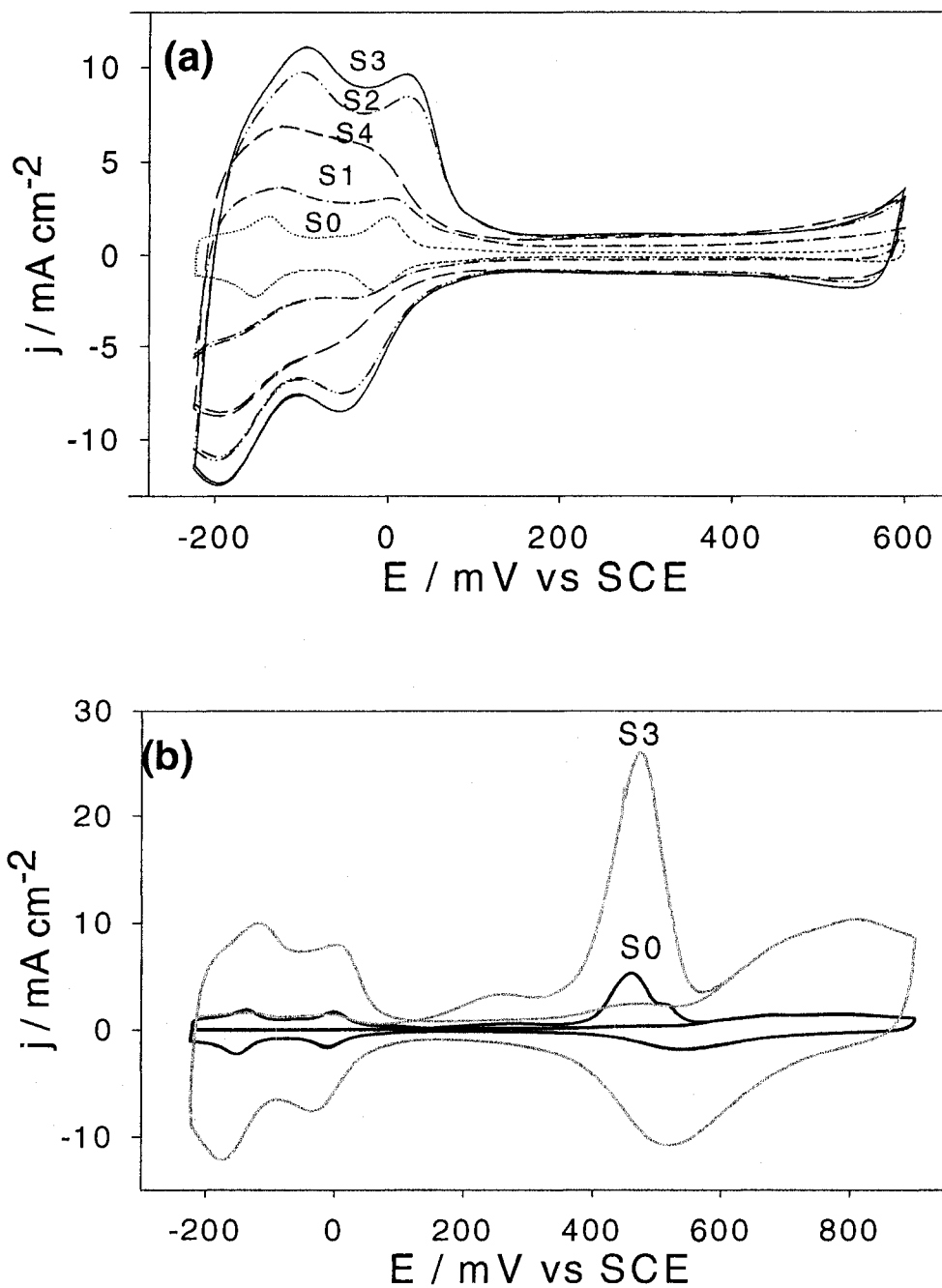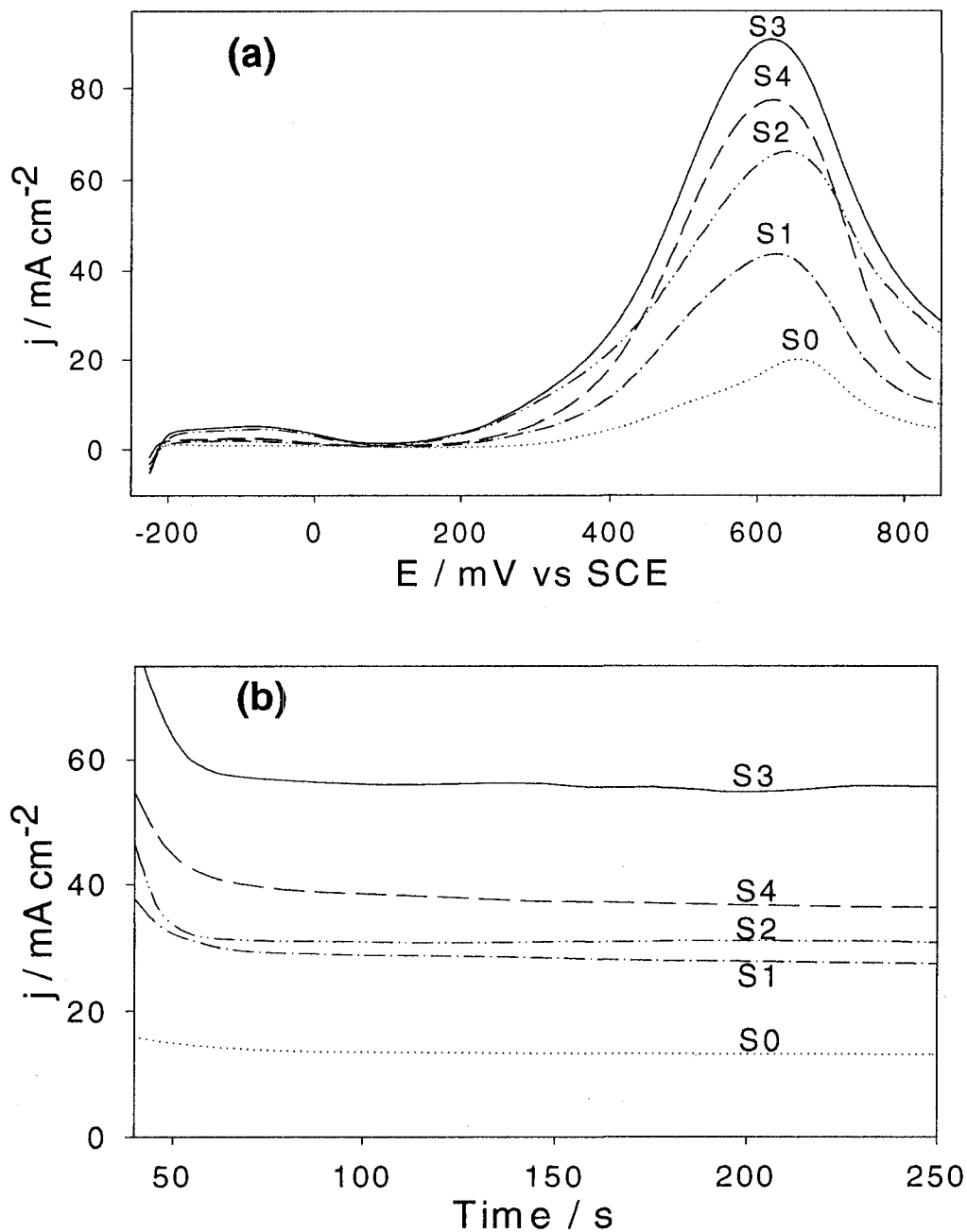
Figure 3.5. Cyclic voltammograms of the (a) S0, S1, S2, S3 and S4 electrodes in 0.5 M H_2SO_4 at a potential scan rate of 20 mV s^{-1}. Cyclic voltammograms of the (b) S0 and S3 electrodes in 0.5 M H_2SO_4 at a potential scan rate of 20 mV s^{-1} after bubbling the solution with CO gas.

3.4 CO Oxidation on the Nanoporous PtIr Networks

Carbon monoxide adsorption and oxidation were studied on the nanoporous PtIr electrodes and the nanoporous Pt electrode. Before the start of the CV experiment, the electrode potential was held at +100 mV for 740 s. First, the CO gas was bubbled into the solution for 600 s to facilitate CO adsorption on the electrode surface, and then the electrolyte was purged with pure Ar for 120 s to remove the excess CO from the electrolyte. Finally, there was a 20 s rest period. As seen in Figure 3.5b, during the first cycle when the potential was scanned from -225 to +200 mV the CV curve is flat, indicating that hydrogen adsorption is completely suppressed by the adsorbed CO. Broad CO oxidation peaks for both electrodes appear between +350 and +550 mV. The earlier onset of CO oxidation shown by the shoulder at +150 mV for the $Pt_{60}Ir_{40}$ electrode and at +350 mV for the nanoporous Pt electrode, and the larger current density in this region demonstrate that the S3 electrode can oxidize CO more efficiently than at the low potentials. The presence of the hydrogen adsorption/desorption peaks and the absence of the CO oxidation peak in the second cycle of the CVs show that the adsorbed CO was completely oxidized during the first cycle. Comparison of the CVs of S3 and S0 further shows that there is a shift in the hydrogen adsorption/desorption peaks. The presence of iridium shifts the hydrogen adsorption peaks to a more negative potential and to the hydrogen desorption peaks to shift positively. The integrated charge for the CO oxidation on S3 is 135.3 $mC\,cm^{-2}$, which is 4.39 times larger than that on S0 (30.83 $mC\,cm^{-2}$). This is consistent with the results presented in Figure 3.5a, further showing the large electroactive surface area of the synthesized nanoporous PtIr electrodes.

3.5 Methanol Oxidation on the Nanoporous PtIr Networks

The electrochemical activity of the nanoporous PtIr electrodes towards the oxidation of methanol is shown in their cyclic voltammetric and chronoamperometric responses. For clarification, only the forward scan of the CVs in 0.1 M CH_3OH + 0.5 M H_2SO_4 at 20 mV s^{-1} are presented in Figure 3.6a. The results illustrate that all the nanoporous PtIr electrodes have much higher current densities and broader peaks than the nanoporous Pt electrode. Also evident in Figure 3.6a, the methanol oxidation starts at a potential of about +300 mV for S0 versus around +150 mV for the nanoporous PtIr electrodes. The current density at low potentials increases significantly in comparison with that of the nanoporous Pt electrode, indicating a much higher activity of the nanoporous PtIr electrodes for the oxidation of methanol. An additional investigation into the electrocatalytic activity of the nanoporous PtIr electrodes was conducted using chronoamperometric measurements at +600 mV as shown in Figure 3.6b. The electrode potentials were held at 0 mV for 60 s, and then stepped up to +600 mV for 300 s. The results in Figure 3.6b demonstrate that all four of the nanoporous PtIr electrodes have much higher steady-state current densities than the nanoporous Pt electrode (S0). The steady-state currents of methanol oxidation are achieved after 200 s. At time of 250 s, the steady-state current densities of the S0, S1, S2, S3, and S4 electrodes are 13.10, 27.56, 30.75, 55.78 and 36.28 mA cm^{-2}, respectively, and thus 2.1, 2.35, 4.26 and 2.77 times higher than that the nanoporous Pt electrode. Therefore, it is evident that the presence of iridium greatly enhances electrocatalysis of Pt towards methanol oxidation. Compared to the other Pt-based bimetallic electrocatalysts we have reported, the nanoporous PtIr electrodes prepared in this study possess superior activity for methanol oxidation [11,20]. This can be attributed to the high electroactive surface area of the formed nanoporous structure and the

Figure 3.6. (a) Forward sweep of the cyclic voltammograms of the S0, S1, S2, S3 and S4

electrodes in 0.5 M H_2SO_4 + 0.1 M CH_3OH at a potential scan rate of 20 mV s^{-1}. (b)

Chronoamperometry of the electrodes in 0.5 M H_2SO_4 + 0.1 M CH_3OH. The potential was

held at 0 mV for 60 s, before being stepped to +600 mV for 300 s.

28

formation of OH_{ads} on Ir at a more negative potentials than on Pt [39]. The OH_{ads} species can facilitate the oxidation of the poisonous intermediates (e.g., CO) formed during the electrochemical oxidation of methanol [11,63].

3.6 Electrochemical Impedance Spectroscopy of Nanoporous PtIr Networks

The Nyquist plots of the S0, S1, S2, S3 and S4 electrodes at the potential of +300 mV in 0.1 M CH_3OH + 0.5 M H_2SO_4 are shown in Figure 3.7a. The frequency was changed from 40 kHz to 25 mHz. The EIS results are consistent with the CV studies shown in Figure 3.6a. Figure 3.7b shows the equivalent electric circuit used to fit the experimental data, where R_s represents the uncompensated solution resistance, R_{ct} the charge transfer resistance and CPE the constant phase element which takes into account methanol adsorption and oxidation [63]. The values for the parameters R_s, R_{ct}, CPE-T, CPE-P are listed in Table 3.1. The error of all the fitting is within ± 4%, indicating that the model can effectively fit the EIS data. S0 has the lowest CPE-T value and S3 has the highest value, which is consistent with the electroactive surface area measurements conducted with hydrogen adsorption/desorption. Out of the four nanoporous PtIr electrodes, S3 exhibits the lowest R_{ct}, which is consistent with the results of cyclic voltammetric and chronoamperometric measurements shown in Figure 3.6. All these results show that the nanoporous $Pt_{60}Ir_{40}$ electrode has high electrocatalytic activity for methanol oxidation.

3.7 ORR Activity of Nanoporous PtIr Electrocatalysts

The typical linear polarization curves for the nanoporous Pt and PtIr electrodes are shown in Figure 3.8. The ORR activity of the electrodes was investigated using linear voltammetry at a potential scan rate of 5 mV s^{-1} in an O_2-saturated solution of 0.5 M H_2SO_4 while continually bubbling O_2 during the experiment to keep the solution saturated. As
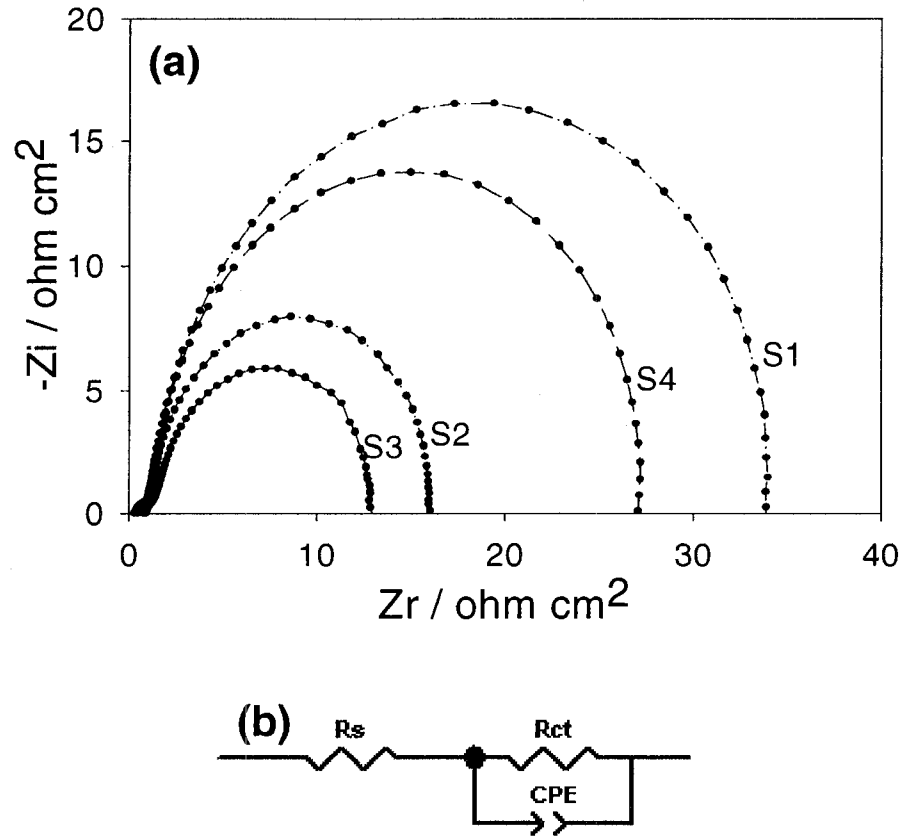
Figure 3.7. (a) Electrochemical impedance spectroscopy (dotted lines) of the nanoporous

PtIr electrodes at a potential of +300 mV in 0.5 M H_2SO_4 + 0.1 M CH_3OH. The amplitude

modulation potential was 10 mV. The frequency was changed from 40 kHz to 25 mHz. (b)

The equivalent electric circuit used to fit the impedance spectra.

Table 3.1. Impedance components for S0, S1, S2, S3, and S4 at +300 mV from fitting the
experimental data with the electrical circuit presented in Figure 3.7.

	S0	S1	S2	S3	S4
R_s	1.83 ± 1.15 %	0.91 ± 1.9 %	0.98 ± 2.4 %	0.88 ± 1.5 %	0.95 ± 1.0 %
R_{ct}/ Ω cm^{-2}	377.1 ± 1.33 %	34.5 ± 1.5 %	15.7 ± 1.5 %	13.7 ± 2.8 %	27.8 ± 1.6 %
CPE-T / μF cm^{-2}	0.0032 ± 0.95 %	0.0062 ± 2.3 %	0.016 ± 2.5 %	0.024 ± 4.0 %	0.016 ± 1.8 %
CPE-P	0.99 ± 0.29 %	0.94 ± 0.6 %	0.96 ± 0.9 %	0.80 ± 1.4 %	0.95 ± 0.6 %

shown in Figure 3.8, the current densities of the ORR for the nanoporous PtIr electrodes are much higher than that for the nanoporous Pt electrode, and the current densities increase with increasing the Ir content from 15% to 40%. However, the current density of the ORR decreases when the Ir content was further increased to 50%. As the electrode potential scans from +850 to +550 mV, the current of the oxygen reduction dramatically increases for all the nanoporous PtIr electrodes and reaches a plateau (the mass transfer limited current) at +550 mV, where the current densities of the ORR for S0, S1, S2, S3 and S4 are 1.06, 1.72, 2.43, 4.12 and 3.00 mA cm^{-2}, respectively. The mass transfer limited current of the nanoporous $Pt_{60}Ir_{40}$ electrode for oxygen reduction is about 4 times larger than that of the nanoporous Pt electrode. In addition, comparison of the curve for the nanoporous Pt electrode (S0) with the curves for the nanoporous PtIr electrodes (S1 – S4) shows that the presence of Ir significantly shifts the onset of oxygen reduction to more positive potentials, indicating a large decrease in the activation energy of the electrochemical reduction of O_2. These two characteristics are evidence for the role of Ir in the catalytic reduction of oxygen, demonstrating that the presence of Ir greatly enhances the electrocatalytic activity of the electrodes towards ORR. The extraordinary high activity of the synthesized PtIr bimetallic catalyst for the oxygen reduction could be attributed to the following synthetic effects. The ORR is kinetically slow and the adsorption of O_2 on the catalysts site is the rate-determining step [64]. The nanoporous structure of the synthesized PtIr bimetallic catalyst with a superior high electroactive surface area greatly enhances the adsorption and diffusivity of O_2. In addition, the presence of Ir could modify the electronic structure of Pt, increasing the Pt 5d vacancy as demonstrated by Ioroi and Yasuda [63]. The increase of the Pt 5d vacancy results in an
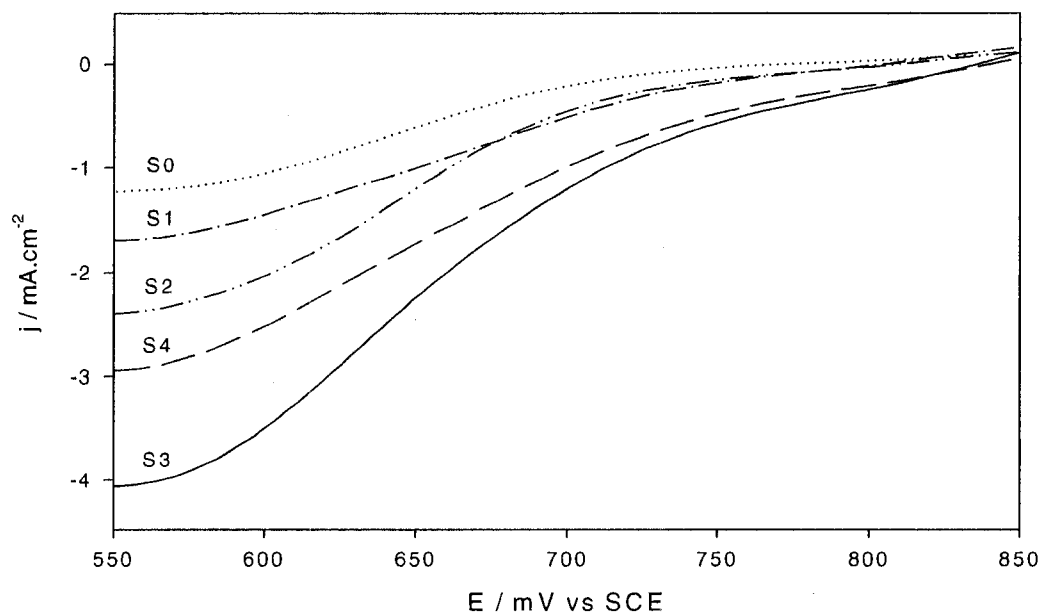
Figure 3.8. Linear voltammograms of the nanoporous PtIr electrodes in 0.5 M H_2SO_4 O_2 saturated solution while continually bubbling O_2 at a potential scan rate of 5 mV s^{-1}.

increased π electron donation from O_2 to the surface Pt, thus increasing the O_2 adsorption and weakening the O-O double bond [65].

3.8. Acid Effect on the Synthesis of Nanoporous PtIr Networks

One of the components used in the synthesis of the PtIr electrocatalysts with the hydrothermal method is hydrochloric acid. Figures 3.9a-c shows the SEM images of the PtIr electrodes made using different concentrations of HCl. All of the other synthesis conditions including temperature and reagent concentration were identical. As the HCl concentration was increased from 0.24 to 0.96 M the particle size increased from tens to hundreds of nanometers. This trend is consistent with a previous study by Chen et al. on fabrication of Pt nanoparticles with varying pHs, where they discovered that the mean size of the particles formed at pH 13, 12 and 10 were 3.0, 4.2 and 9.1 nm, respectively [12]. Methanol oxidation was used as a probe to further investigate the effect of acid concentration on the electrocatalytic performance of the nanoporous PtIr electrocatalysts. Figure 3.9d reveals that as the acid concentration was increased, the peak current density also increased. As electroactive surface area is a determination of the number of catalytic sites available and an indicator of electrocatalytic performance. This would imply that at high acid concentration a greater number of particles were deposited, resulting in the high electrocatalytic performance. In summary, acid concentration in the hydrothermal synthesis of the PtIr electrocatalysts has a significant effect on the amount of particles deposited and particle size.

3.9. Substrate Effect on the Synthesis of Nanoporous PtIr Networks

Graphite and CNT substrates were used to investigate the effect of substrate on deposition and the electrocatalytic performance of the PtIr electrocatalysts. The carbon nanotubes were synthesized via CVD using a two-step process. First Co catalyst particles
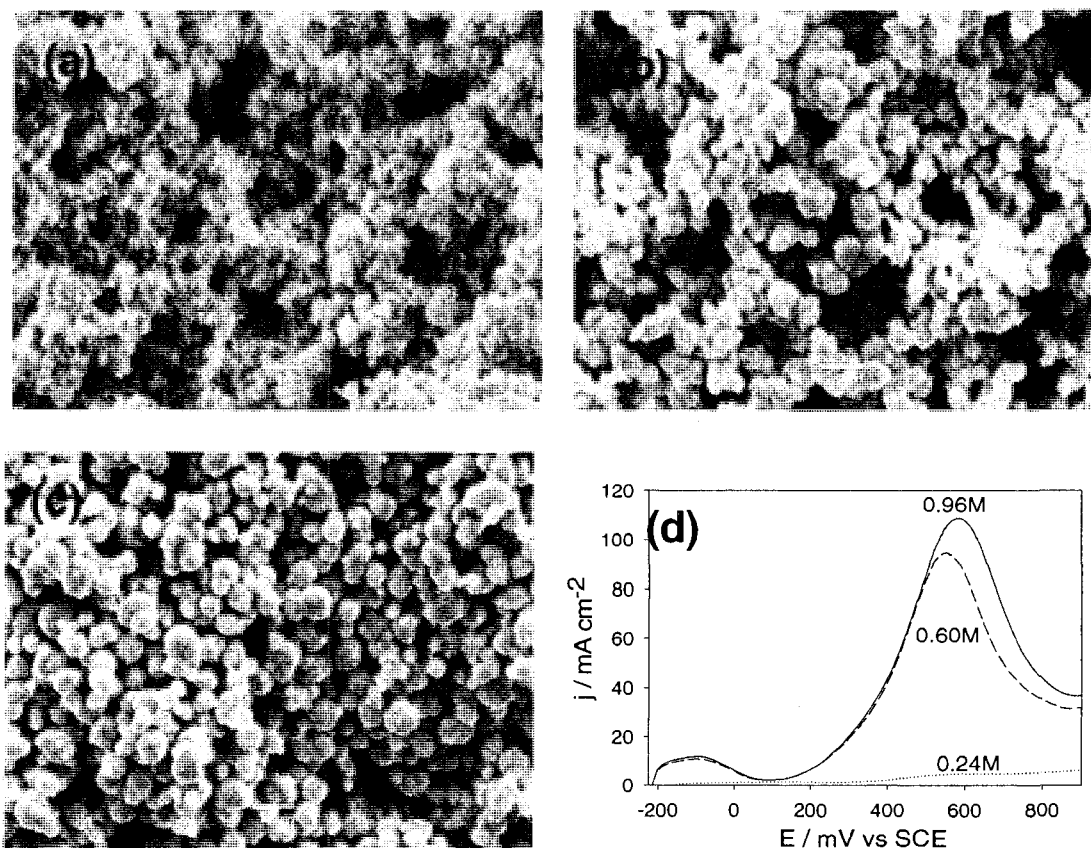
Figure 3.9. SEM images of nanoporous PtIr electrodes fabricated with (a) 0.24 M, (b) 0.60 M and (c) 0.96 M HCl at 10,000x magnification. (d) Forward sweep of the cyclic voltammograms of electrodes in 0.5 M H_2SO_4 + 0.1 M CH_3OH at a potential scan rate of 20 mV s^{-1}.

were deposited onto the graphite surfaces using electrochemical deposition. The graphite was placed into a sealed quartz flow reactor, using acetone as a carbon source and heating to 750 °C for 1.5 h, resulting in the formation of the multiwalled CNTs. The purification and solubilization of the CNTs were the major obstacle to overcome before further experiments could be conducted. The problems with the CNTs produced were two-fold. There were a variety of impurities, including metal catalyst particles, amorphous carbon and smaller fullerenes hindering the electronic properties of the CNTs. Also, the CNTs produced were very hydrophobic which made it difficult to conduct the electrochemical experiments. Two purification techniques were investigated: mild oxidation and acid treatment. In the literature, the CNTs are typically suspended in solution or removed from their substrate prior to purification. This allows for use of strong acids or oxidizers during the purification procedure [71]. However, after the purification procedure, the CNTs have to be reattached to substrate. In order to avoid this step, the CNTs were fabricated directly onto the graphite substrate this study.

Figure 3.10 shows the optical microscopy images of the water contact angle of the CNTs before and after various purification procedures. Figure 3.10a shows the image of an untreated CNT, with a water contact angle of 125°. With a high water contact angle the sample would be unusable for electrochemical experiments; as air bubbles would be present on the electrode surface. Figure 3.10b shows the water contact angle of 30° for CNTs treated with 3.0 M HNO_3 for 3 h. This mild acid treatment had no effect on the CNTs or the carbonaceous impurities, but dissolved the metal catalyst particles. Figure 3.10c shows the water contact angle of 40° for CNTs treated with 3:1 ratio of 3.8 M H_2SO_4 and 7.5% H_2O_2
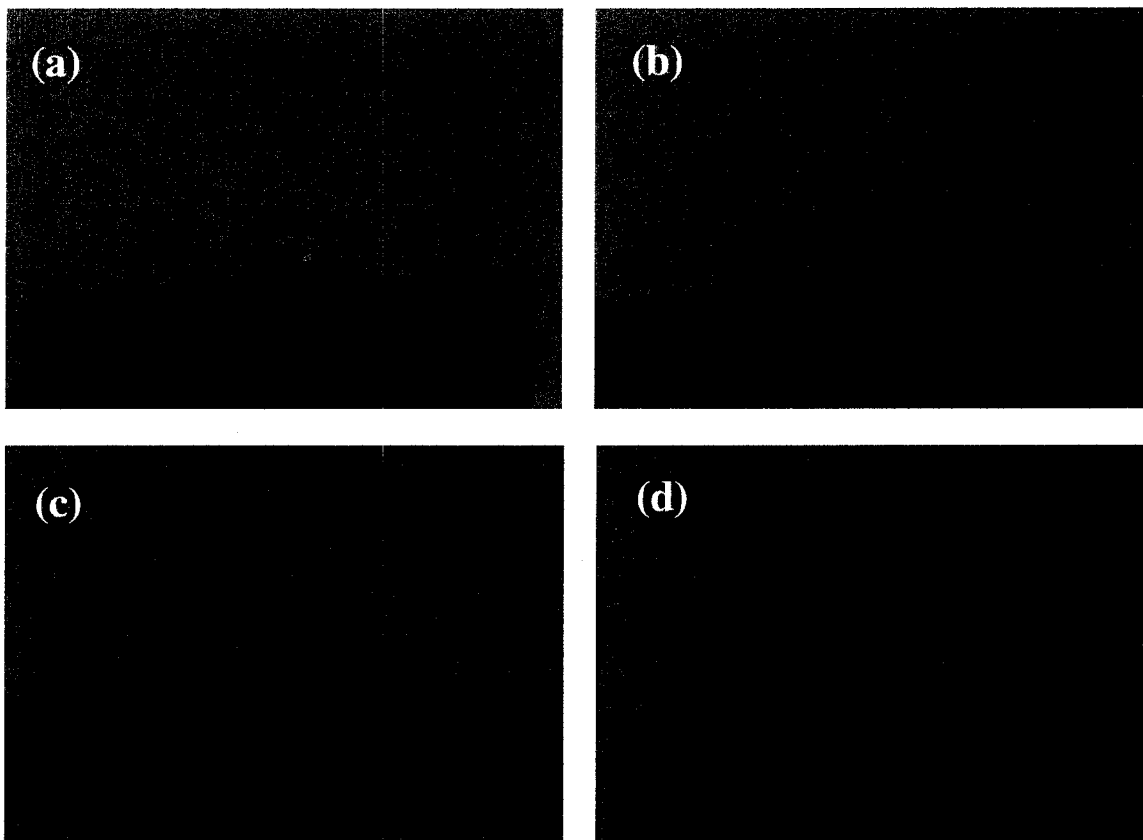
Figure 3.10. Optical microscopy images of the water contact angle of CNTs before and after purification using various procedures: (a) untreated CNTs (b) CNTs after purification in 3.0 M HNO_3 for 3 h, (b) CNTs after purification in 3:1 ratio of 3.8 M H_2SO_4 and 7.5% H_2O_2 for 3 h, (d) CNTs after purification for 1.5 h in each of the above solutions.

for 3 hours. This mild oxidation treatment oxidizes the carbonaceous impurities, while having no effect on the metal catalyst particles. The downside to this treatment is that the CNTs experienced some shortening of the tube length and the consumption of the sidewall defects. Figure 3.10d shows the water contact angle resulting from treatment in each solution for 1.5 h. The water contact angle of 10° was the best observed for any of the purification procedures. With the CNTs sufficiently solubilized with a water contact angle of 10° and a large portion of the metal and carbonaceous impurities removed further experiments can be conducted.

Nanoporous PtIr electrocatalysts were deposited on to the CNT and graphite surfaces using conditions similar to the hydrothermal method described in the experimental section. The graphite and CNT substrates take up a significantly larger volume in the Teflon® vessel than the Ti plates, which necessitated reducing the overall volume of the solution, and, thus the concentration of all the reagents to 75% of their original values. The SEM images of the CNT/PtIr electrode are shown in Figures 3.11a-d. As is evident in Figures 3.11a & b, the nanoporous PtIr electrocatalysts possesses the same network structure as the previously fabricated PtIr electrodes and the surface coverage is slightly lower due to the reduction in the concentration of the reagents. Figure 3.11c & d reveal that the CNTs have a spaghetti-like structure and the as-synthesized PtIr electrocatalysts sit on top of the CNTs. A variety of electrochemical experiments were conducted to assess the performance of the CNT and graphite substrates. Figure 3.12a shows the CVs with the two electrodes in 0.5 M H_2SO_4 at a potential scan rate of 20 mV s^{-1}. Integrating the intensity of the hydrogen adsorption peaks reveals the that electroactive surface areas of the graphite/PtIr and CNT/PtIr electrodes are
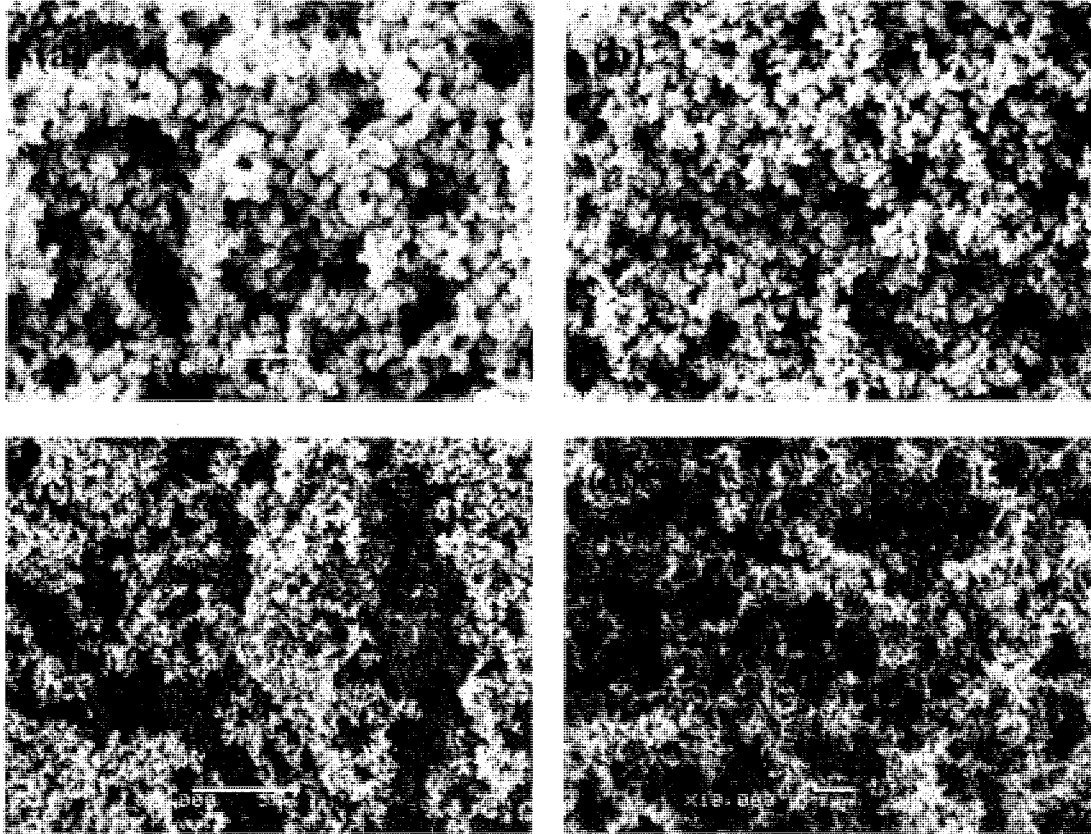
Figure 3.11. SEM images of the as-synthesized CNT/PtIr electrodes at (a) 15,000x, (b) 10,000x, (c) 5,000x and (d) 10,000x magnification.

24.75 and 42.15 mA cm^{-2}, respectively, indicating the increased electroactive surface area of the CNT/PtIr electrode.

The electrocatalytic activity of the two electrodes towards the oxidation of methanol is shown in the cyclic voltammetry and chronoamperometric responses. For clarification, only the forward scan of the CVs in 0.5 M H$_2$SO$_4$ + 0.1 M CH$_3$OH at a potential scan rate of 20 mV s^{-1} is presented in Figure 3.12b. The results illustrate that the CNT/PtIr electrode has higher current density throughout the potential range versus the graphite/PtIr electrode, indicating the higher activity of the CNT/PtIr electrode for methanol oxidation.

An additional investigation into the electrocatalytic activity of the electrodes was conducted using chronoamperometric measurements at +300 mV as shown in Figure 3.12c. The steady-state currents of methanol oxidation are achieved after 200 s. At a time of 250 s, the steady-state current densities for the graphite/PtIr and CNT/PtIr electrodes are 3.1 and 4.5 mA cm^{-2} respectively, demonstrating that the CNT/PtIr electrode possesses superior activity for methanol oxidation. Since the hydrothermal conditions used in each synthesis were identical, the higher activity of the CNT/PtIr electrode can be attributed to the high surface area CNT supporting material.

The Nyquist plots for the graphite/PtIr and CNT/PtIr electrodes at a potential of +300 mV in 0.5 M H$_2$SO$_4$ + 0.1 M CH$_3$OH are shown in Figure 3.12d. The inset of Figure 3.12d shows the equivalent electric circuit used to fit the experimental data. The elements of the circuit are the same as previously discussed in Section 3.6. The fitting error is within ±2%, indicating that the model can effectively fit the data. The corresponding R$_{ct}$ values for the graphite/PtIr and CNT/PtIr electrodes were 26.98 and 16.89 Ω cm^{-2}, respectively, which is consistent with the results of cyclic voltammetric and chronoamperometric measurements
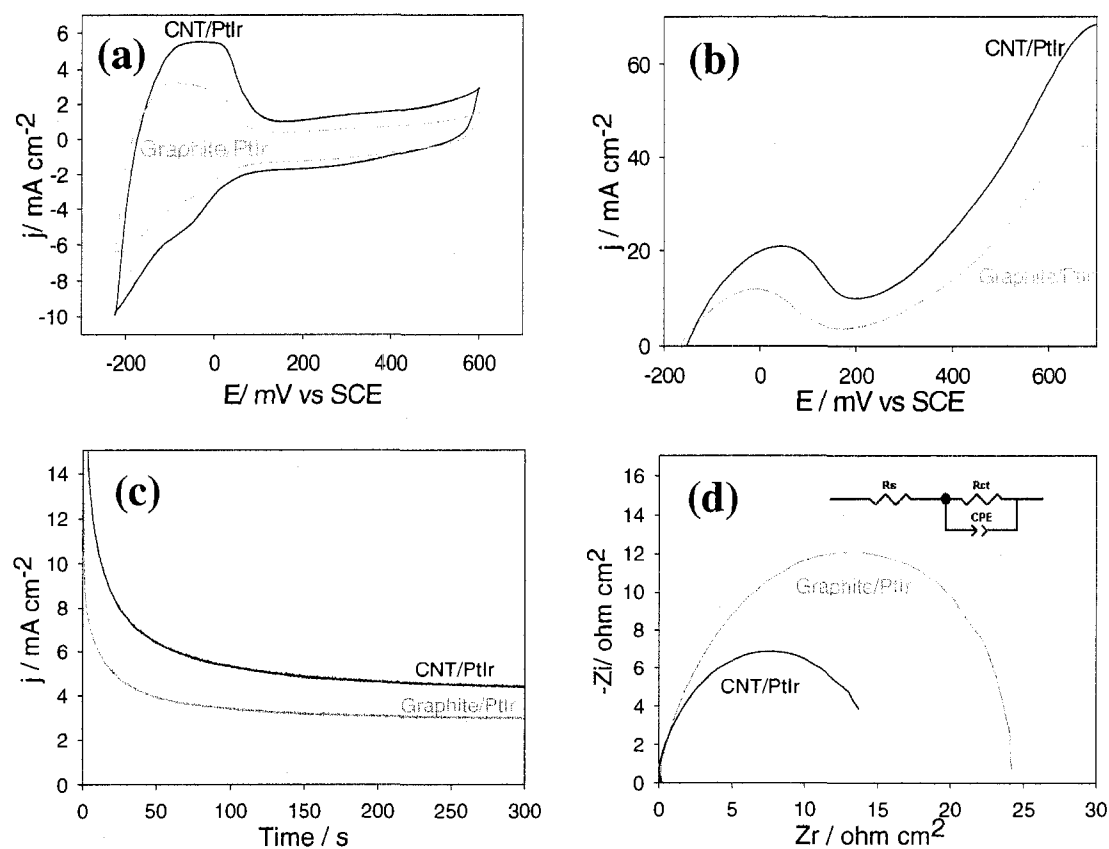
Figure 3.12. Comparison of CNT/PtIr and graphite/PtIr electrodes. (a) Cyclic voltammograms of the electrodes in 0.5 M H_2SO_4 at a potential scan rate of 20 mV s^{-1}. (b) Forward sweep of the cyclic voltammograms of electrodes in 0.5 M H_2SO_4 + 0.1 M CH_3OH at a potential scan rate of 20 mV s^{-1}. (c) Chronoamperometry of the electrodes in 0.5 M H_2SO_4 + 0.1 M CH_3OH. The potential was held at 0 mV for 60 s, before being stepped to +300 mV for 300 s. (d) Electrochemical impedance spectroscopy of the electrodes at a potential of +300 mV in 0.5 M H_2SO_4 + 0.1 M CH_3OH. The amplitude modulation potential was 10 mV. The frequency was changed from 40 kHz to 25 mHz.

40

shown in Figures 3.12a-c. Overall higher current densities were observed for the CNT/PtIr electrode than the graphite/PtIr electrode, demonstrating the larger electroactive surface area of the electrode, which is consistent with a previous study by Liao et al. that investigated the electrocatalytic activity of Pt-based nanoparticles dispersed onto XC-72R and CNT substrates [72]. The high surface area of the CNTs is a desirable property for electrode supporting materials.

3.10 Methanol Oxidation on the Nanoporous Pt-based Networks

Electrocatalysts were formed using the hydrothermal method with equivalent concentrations of the platinum precursor to form various bimetallic Pt-based nanomaterials with atomic ratios close to 50:50. The electrocatalytic activity of the nanoporous Pt-based electrocatalysts towards methanol oxidation was studied using cyclic voltammetry. Figure 3.13a shows the forward sweep of the CVs in 0.1M H_2SO_4 + 0.1M CH_3OH at a potential scan rate of 20 mV s^{-1}, from which it is evident that all five of the nanoporous Pt-based electrodes have significantly enhanced current densities over the polycrystalline Pt electrode. The peak current densities of the electrodes increase in the order of polycrystalline Pt < nanoporous Pt < PtRu < PtPd < PtPb < PtIr. In terms of the ability to oxidize methanol at low potentials, the PtIr electrode is second only to the PtRu electrode, but has a peak current density over 3.5 times higher. Comparison of the same data, but with reference to the electroactive surface areas in Figure 13.3b, shows that the PtIr electrode outperforms the other electrodes in terms of current density. This demonstrates that the incorporation of Ir into Pt-based electrodes increases the intrinsic electrocatalytic activity of the electrode towards methanol oxidation [59].
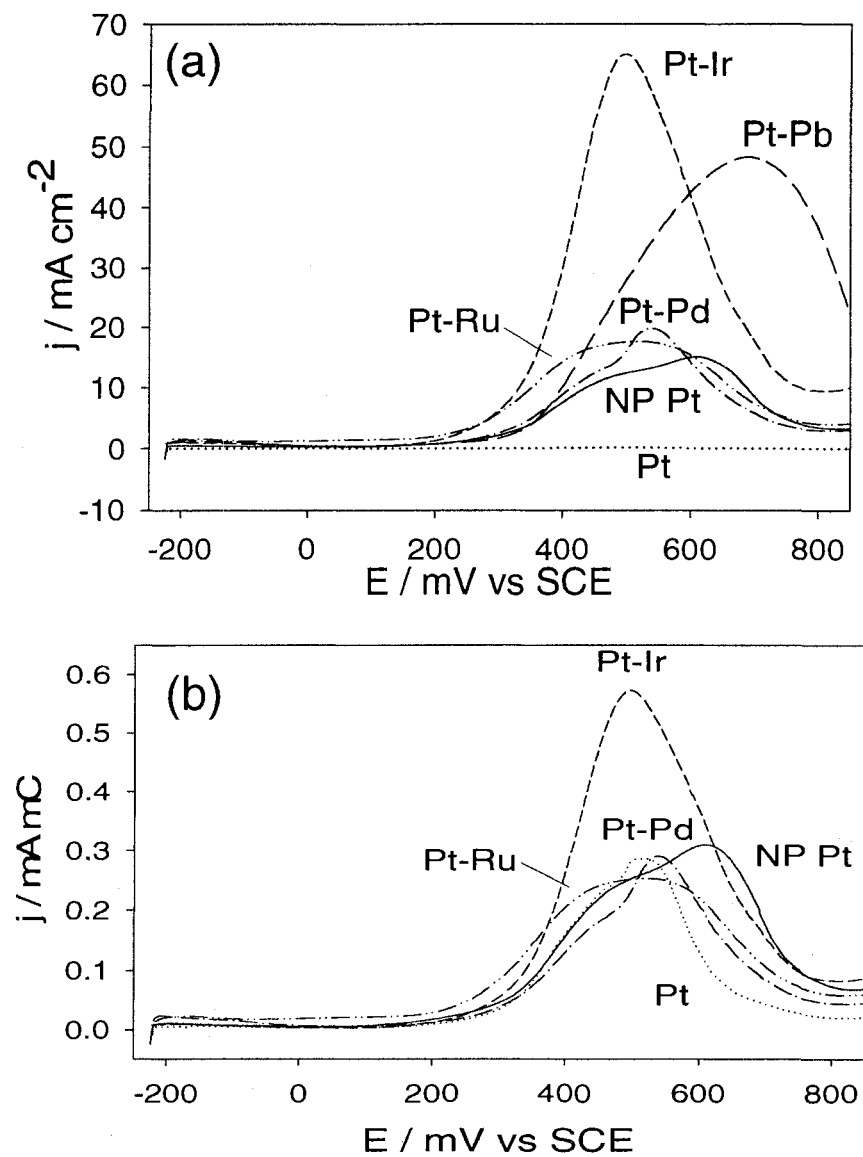
Figure 3.13. Forward sweep of the cyclic voltammograms of different bimetallic Pt-based electrodes in 0.1 M H_2SO_4 + 0.1 M CH_3OH at a potential scan rate of 20 mV s^{-1}. The figures show the current density calculated from the (a) geometric and (b) electroactive surface areas [59].

3.11 Summary

Nanoporous PtIr electrodes with different ratios of Pt to Ir were prepared using a one-step facile hydrothermal method. Formaldehyde was used as the reduction agent to simultaneously reduce Ir^{3+} and Pt^{4+}, resulting in the formation of bimetallic PtIr nanoporous structures. The hydrogen adsorption/desorption experiments reveal that the synthesized nanoporous PtIr electrodes possess extraordinarily high active surface area. Subsequent electrochemical studies show that the presence of Ir dramatically improves the electrocatalytic activity of Pt towards the electrochemical oxidation of CO and methanol and the electrochemical reduction of oxygen. Among the four synthesized nanoporous PtIr electrodes, $Pt_{85}Ir_{15}$, $Pt_{72}Ir_{28}$, $Pt_{60}Ir_{40}$ and $Pt_{50}Ir_{50}$, the nanoporous $Pt_{60}Ir_{40}$ electrode exhibits the largest electroactive surface area, the lowest charge-transfer resistance and the highest electrochemical activity. The steady-state current density of the nanoporous $Pt_{60}Ir_{40}$ electrode for methanol oxidation at 0.6 V is over four times higher than that of the nanoporous Pt electrode, and the mass transfer limited current of the nanoporous $Pt_{60}Ir_{40}$ electrode for oxygen reduction is about four times larger than that of the nanoporous Pt electrode. Acid concentration was shown to have a significant effect on the number and size of the PtIr catalyst particles deposited on the surface. PtIr electrocatalysts were successfully deposited onto the CNT and graphite substrates, with the resulting CNT/PtIr electrode showing enhanced electrocatalytic activity towards methanol oxidation due to a larger electroactive surface area. The hydrothermal method used in the fabrication of the PtIr electrocatalysts is a powerful technique whereby the synthesis parameters can be easily tuned to achieve optimum deposition, particle size and composition. In comparison to other bimetallic Pt-based electrocatalysts fabricated with the same hydrothermal method, PtIr shows the highest

electrocatalytic activity towards methanol oxidation, which demonstrates its potential for applications in electrochemical energy conversion.

Chapter 4

Amperometric Glucose Sensor Based on Bimetallic Pt-Ir Nanomaterials

4.1 Introduction

Previous and current research has focused on the development of novel glucose

sensors with fast response, long lifetimes, high sensitivity and selectivity. The

electrochemical oxidation of glucose is the key reaction considered in the fabrication of

glucose biosensors. In literature, two distinct types of catalysts have emerged with the

potential for application in commercial glucose sensors: enzymatic and non-enzymatic.

Enzyme based glucose sensors are fabricated by immobilizing an enzyme onto a supporting

electrode. The application of enzymatic biosensors has been hindered by the thermal and

chemical instabilities of the enzymes as well as by complex immobilization procedures that

may further decrease the stability of the enzyme. Some research has focused on retaining and

increasing the activity of the enzyme, whereas other research has focused on the development

of non-enzymatic catalysts. Studies on the kinetics and mechanism of glucose electro-

oxidation on pure platinum surfaces revealed that Pt electrodes suffer from low sensitivity,

poor selectivity and poisoning from interfering species [73,74]. A variety of Pt-based

bimetallic materials (Bi, Pb, Tl, W) have been fabricated with the goal of improving the

sensitivity and selectivity of the electrodes towards the electro-oxidation of glucose [51-54].

Nevertheless, the application of these sensors is hindered by the toxicities of heavy metal

elements. Iridium and iridium oxide have been employed in enzymatic glucose sensors due to

their biocompatibility, stability and excellent electrical conductivity. Several studies have

investigated the effect of the addition of Ir or IrO_2 in amperometric glucose sensors with

glucose oxidase as the catalyst. The resulting sensors exhibited good stability and increased

the sensitivity towards glucose via the detection of hydrogen peroxide at low potentials where the response from common interferences species is low [56-58].

4.2 Characteristics of PtIr Electrodes for Glucose Sensing

The surface morphology of the prepared Pt and PtIr electrodes was characterized using SEM. The hydrothermal method used in the fabrication of the nanoporous Pt and PtIr networks is the similar to the one previously reported [61], apart from the optimization of pH and reagent concentrations. Figures 4.1a-c present the SEM images of fabricated PtIr materials. All of the prepared Pt and PtIr electrodes possess a nanoporous network structure. As is evident from the images, the titanium substrate is completely covered by catalyst particles ranging, in size from 50-700 nm. EDS analysis was performed to determine the composition of the samples: S5, Pt; (b) S6, $Pt_{78}Ir_{22}$; and (c) S7, $Pt_{62}Ir_{38}$.

Cyclic voltammograms for the S5, S6 and S7 electrodes in 0.5 M H_2SO_4 at a sweep rate of 20 mV s^{-1}, were used to analyze the characteristics of hydrogen adsorption and desorption as shown in Figure 4.1d. All the electrodes exhibit similar hydrogen adsorption and desorption characteristics, as evident by the two peaks on the forward and reverse scans. The current density of the peaks increased with increasing iridium content, which is consistent with the results presented in Chapter 3. The electroactive surface area was calculated by integrating the intensity of the hydrogen adsorption and desorption peaks. The charges for the S5, S6 and S7 electrodes were determined to be 14.0, 98.4 and 137.96 mA cm^{-2}, respectively.
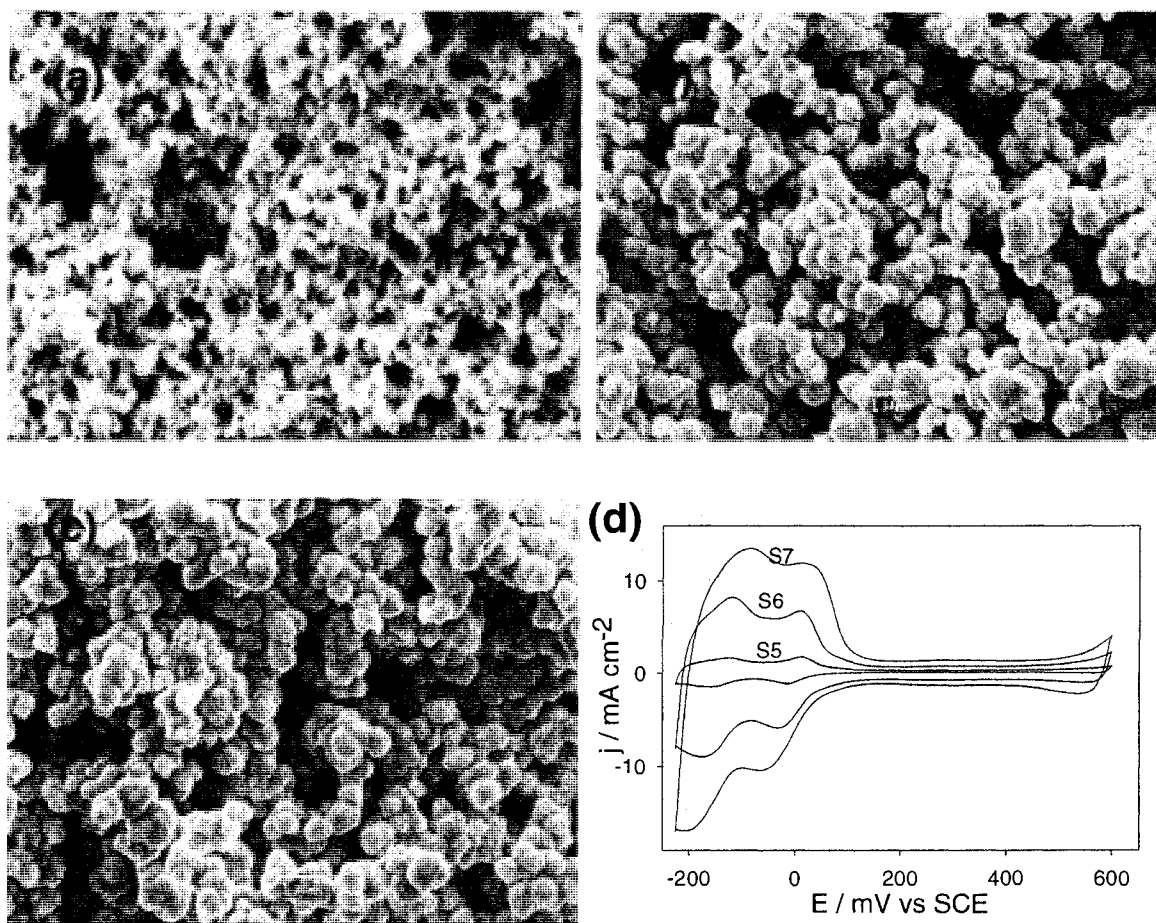
**Figure 4.1.** SEM images: (a) nanoporous Pt (S5), nanoporous $Pt_{78}Ir_{22}$ (S6), nanoporous $Pt_{62}Ir_{38}$ (S7) at 10,000x magnification. Cyclic voltammograms of the S5, S6 and S7 electrodes in 0.5 M H_2SO_4 at a potential scan rate of 20 mV s^{-1}.

4.3 Electro-oxidation of Glucose in Neutral Media

The catalytic properties of the as-synthesized electrodes were investigated using voltammetric methods. For clarification, only the forward scans are presented. In the interest of developing novel electrode catalysts suitable for application in glucose biosensors, a pH 7.4 phosphate buffer solution was chosen as the electrolyte and added chloride ions, which are known to suppress glucose adsorption and decrease the oxidation rate on a pure Pt electrode. Figure 4.2a, presents the forward scan of the CVs of the S5, S6 and S7 electrodes in 0.1 M phosphate buffer (pH 7.4) + 0.15 M NaCl + 5 mM glucose at a potential scan rate of 10 mV s^{-1}. Even in the presence of the chloride ion, all three electrodes exhibit good catalytic activity as is evident by the multiple anodic peaks attributed to the oxidation of glucose and its intermediates. The PtIr electrodes S6 and S7 exhibit two different characteristics from the nanoporous Pt electrode. The oxidation peaks at around -300 and +100 mV become much broader and the current density is enhanced with the increasing iridium content of the electrodes. This indicates that the $Pt_{62}Ir_{38}$ electrode exhibits the best catalytic activity of the three electrodes.

Figures 4.2b-d show the response of the nanoporous Pt and PtIr electrodes towards the electro-oxidation of glucose. All three electrodes exhibit increasing current density as the concentration of glucose, that is, due to the oxidation of glucose on the electrode surfaces. The CVs reveal three distinct regions. At low potential an oxidation peak emerges at -300 mV and broadens with increasing glucose concentrations, which could be attributed to the electrosorption of glucose forming glucose intermediates like the enediol type [48]. The formation of these intermediates could inhibit the further electrosorption of glucose,

48
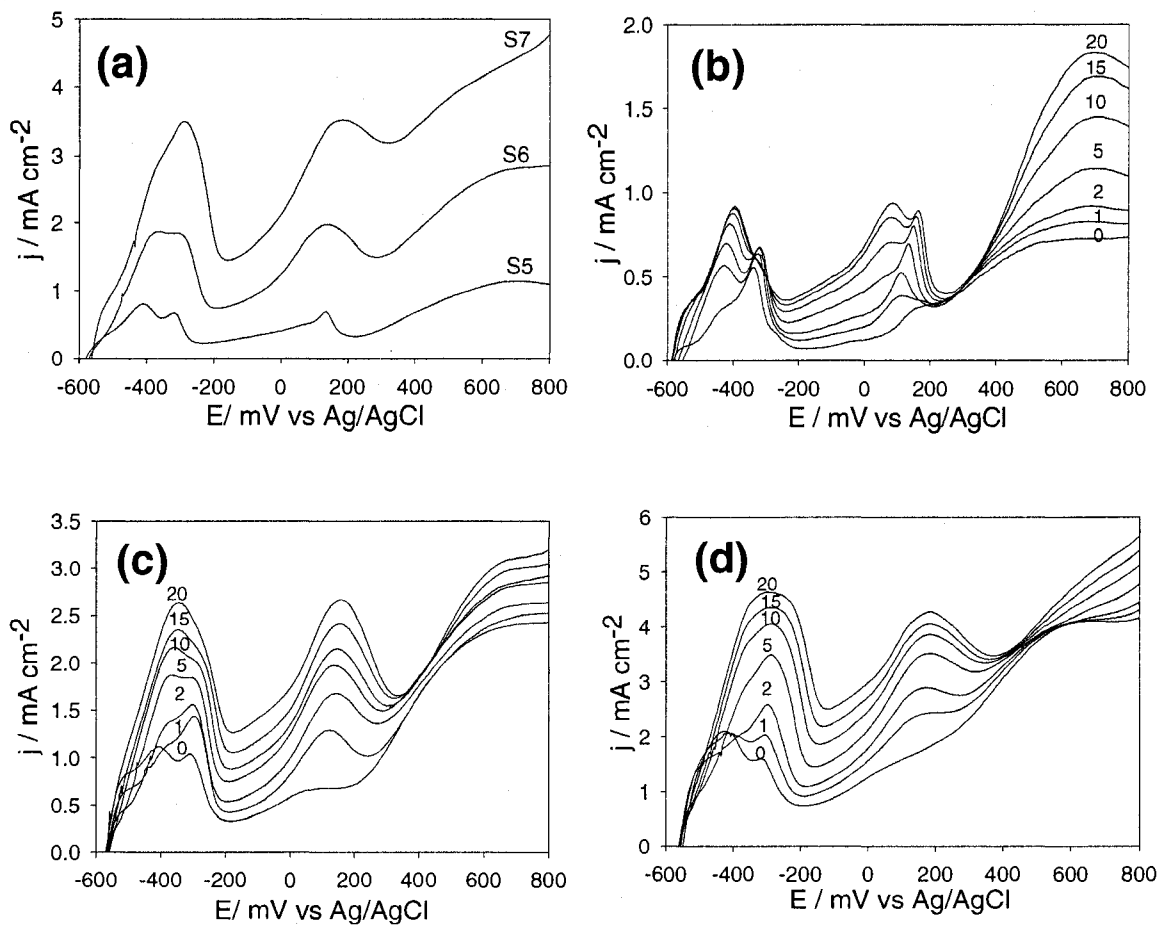
**Figure 4.2.** Positive sweep of cyclic voltammograms in 0.1 M phosphate buffer (pH 7.4) + 0.15 M NaCl solution at 10mV s⁻¹. (a) S5, S6 and S7 electrodes with 5mM of glucose. (b) S5, (c) S6 and (d) S7 electrodes with 0, 1, 2, 5, 10, 15, 20 mM glucose.

resulting in the decrease in current at -175 mV. Another oxidation peak occurs at about +200 mV, perhaps due to the oxidation of the intermediate layer and the partial oxidation of glucose. At potentials above +300 mV, the complete oxidation of glucose and its intermediates may occur forming products such as gluconolactone or gluconic acid [48]. Overall, the S7 electrode shows good catalytic activity towards the electro-oxidation of glucose and its intermediates at different concentrations of glucose and potentials in neutral media and in the presence of the poisoning chloride ion. This will allow us to choose the potentials to be used for the amperometric sensing of glucose.

4.4 Amperometric Response towards Glucose under Physiological Conditions

The three distinctive regions that show current responses to increasing concentrations of glucose were chosen as the potentials for amperometric testing. Figure 4.3a compares the amperometric responses of the S7 electrode at -300, +100 and +600 mV upon successive 1 mM additions to the glucose concentration (from 0-20 mM). After each injection of glucose to the stirred solution the current increases rapidly and sensitively. At a current density of -300 mV, the current density tends to drop off a small amount after each 1 mM addition of glucose. By contrast, the current responds in a linear manner with incremental glucose addition at +100 and +600 mV. At a low potential of -300 mV, glucose cannot be completely oxidized and the formation of intermediates on the electrode surface blocks some of the active surface sites, causing the nonlinear chronoamperometric response to glucose concentration. This feature is more evident in the calibration curves in Figure 4.3b which shows that, above glucose concentrations of 10 mM, the current density starts to drop at a potential of -300 mV, whereas at potentials of +100 and +600 mV a linear relationship is evident. The linear chronoamperometric responses of the S2 electrode at the potentials of
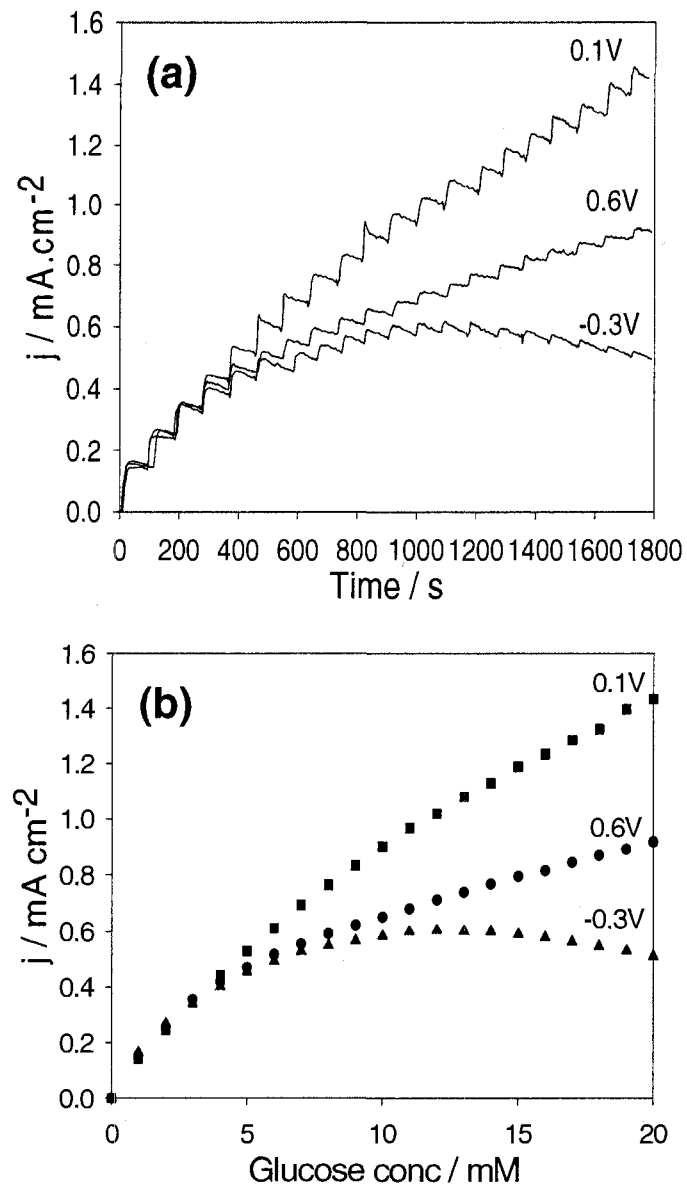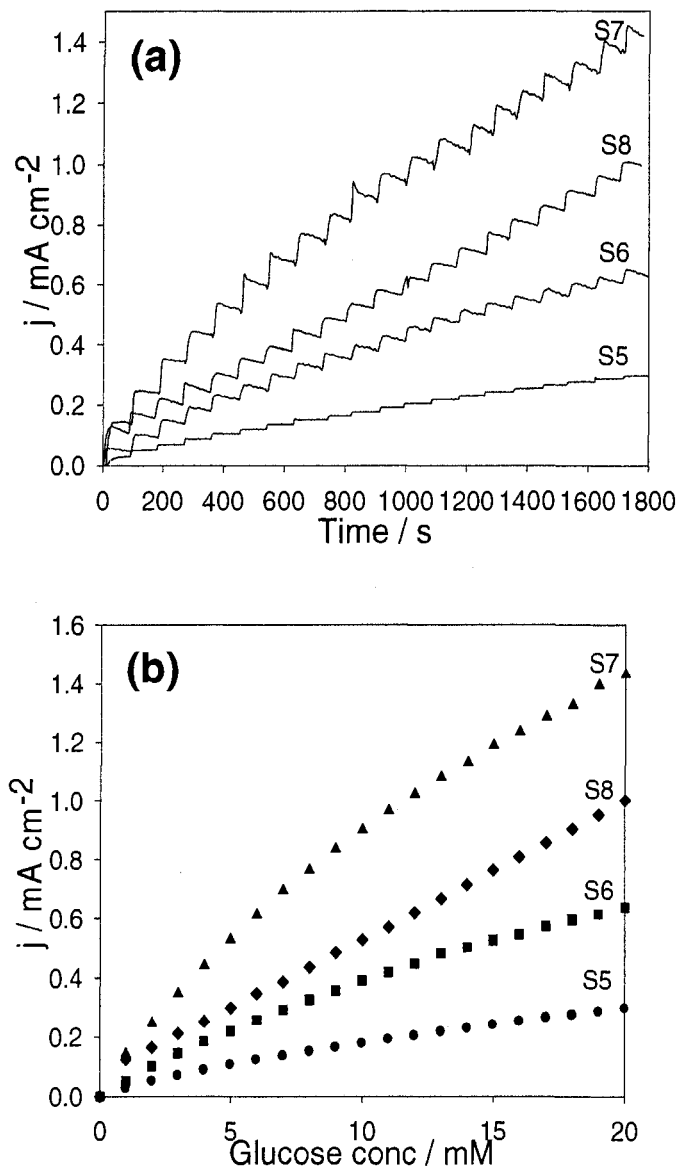
Figure 4.3. (a) Chronoamperometry curves and (b) calibration plots at -300, 100 and 600 mV

for the S7 electrode in 0.1 M phosphate buffer (pH 7.4) + 0.15 M NaCl solution with

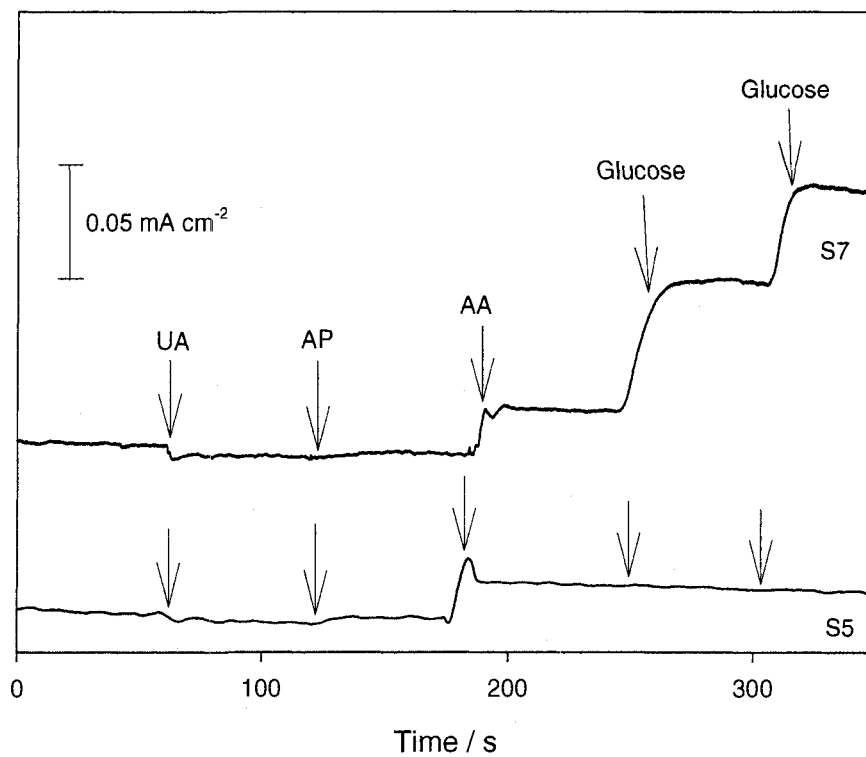successive additions of 1 mM glucose (from 0-20 mM) every 90 s .

+100 and +600 mV indicates glucose and its intermediates can be continuously oxidized on the PtIr surface. While the steady-state chronoamperometric experiments revealed the current density for +600 mV was double that for +100 mV, the current response and sensitivities in the amperometric detection of glucose were higher at +100 mV, indicating that platinum oxide formation contributes to the current density at high potentials. Previous studies have indicated that the optimum potential for the sensing of glucose on Pt surfaces such as mesopores and nanotubule arrays was +400 mV [46,75]. This observed shift in the optimum potential required for maximum sensitivity in the detection of glucose is attributed to the high electrocatalytic activity of the PtIr electrode for the electro-oxidation of glucose.

The amperometric detection of glucose at the optimum potential of +100 mV was investigated with the nanoporous Pt, $Pt_{78}Ir_{22}$ and $Pt_{62}Ir_{38}$ electrodes to determine the optimum electrode materials for glucose sensing. A $Pt_{47}Ir_{53}$ electrode, denoted by S8, was added for comparison purposes. As shown in Figure 4.4a, all three of the electrodes have linear chronoamperometric responses to glucose concentration within physiological conditions. The calibration plots in Figure 4.4b indicate that the amperometric sensitivities increase in the following order: $Pt < Pt_{78}Ir_{22} < Pt_{47}Ir_{53} < Pt_{62}Ir_{38}$, with values of 18.7, 40.2, 54.1 and 93.7 µA cm^{-2} mM^{-1}, respectively. Therefore the optimum bimetallic ratio of Pt:Ir for the detection of glucose is 62:38.

As previously discussed, one of the major challenges in non-enzymatic glucose detection is the interfering electrochemical signals caused by the oxidation of endogenous species substances such as UA, AP and AA at the electrode surface. Figure 4.5 presents the selectivity testing results for the Pt and $Pt_{62}Ir_{38}$ electrodes with successive additions of UA, AP, AA and glucose in 0.1 M PBS solution containing 0.15 M NaCl at +100 mV. Both the

Figure 4.4. (a) Chronoamperometry curves and (b) calibration plots at 100 mV for the S5,

S6, S7 and S8 electrodes in 0.1 M phosphate buffer (pH 7.4) + 0.15 M NaCl solution with

successive additions of 1mM glucose (from 0 to 20 mM) every 90 s.

Figure 4.5. Chronoamperometry curves of the S5 and S7 electrodes in 0.1 M PBS + 0.15M

NaCl solution with successive additions of 0.2 mM UA, 0.1 mM AP, 0.1mM AA and 1 mM

glucose at 60 s intervals with a potential of +100 mV.

S5 and S7 electrodes exhibit similar responses to the addition of the interference species, with AA producing the only significant change in current. Interestingly, the S7 produces a significant response to the subsequent additions of glucose, whereas the S5 electrode did not survive the impact of the interfering species.

4.5 Summary

In summary, the amperometric responses of nanoporous PtIr electrodes with different compositions towards glucose were tested in neutral media. The PtIr electrodes have strong and sensitive current responses to glucose at a variety of potentials. At a potential of +100 mV the $Pt_{62}Ir_{38}$ electrode exhibits very strong and sensitive amperometric responses to glucose even in the presence of a high concentration of the chloride ion and other common interfering species. Ease of fabrication, fast response and high sensitivity make the nonenzymatic glucose sensor proposed in this study a very promising candidate for application in the commercial detection of glucose.

Chapter 5

Enhancement of Nanoporous PtRu Networks with Iridium

5.1 Introduction

The formation of CO on Pt-based anodes reduces the overall efficiency of DMFCs to about 27%, thereby making CO poisoning one of the major limitations hindering the practical applications in DMFCs. A variety of co-catalysts such as Mo [21], Ru [17-20], Sn [25-27] and W [22,23] have been coupled with Pt to enhance CO oxidation. To date, the best results have been achieved using Ru [17-20]. In particular, the nanoporous $Pt_{62}Ru_{38}$ electrocatalyst fabricated by Koczkur et al. exhibited high electrocatalytic activity towards methanol and CO oxidation [78]. Given the proposed mechanism by which Ru enhances CO oxidation via the generation of oxygen-like species, the addition of an oxygen evolution catalyst such as IrO_2 may enhance the electrocatalytic activity of PtRu towards CO and methanol oxidation. The initial results on the fabrication and electrocatalytic activity of the nanoporous PtRuIr electrocatalyst are presented.

5.2 Surface Characterization of the Nanoporous PtRuIr Networks

The hydrothermal method is a powerful fabrication technique allowing the composition of bimetallic PtM (M= Ru, Ir) electrocatalysts to be easily changed by varying the concentration of the Pt or M precursors. In spite of this, the fabrication of the nanoporous PtRu and PtIr electrocatalysts were much different with PtRu requiring low concentrations of HCl and formaldehyde and PtIr utilizing high concentrations of both components. The composition of the as-synthesized PtRuIr electrocatalyst was found to be more dependent on the concentration of HCl and formaldehyde than on the concentrations of the Pt, Ru or Ir precursors.

The surface morphology of the as-synthesized PtRu and PtRuIr electrodes was characterized using SEM. As evident from the images in Figure 5.1a and b, the bimetallic
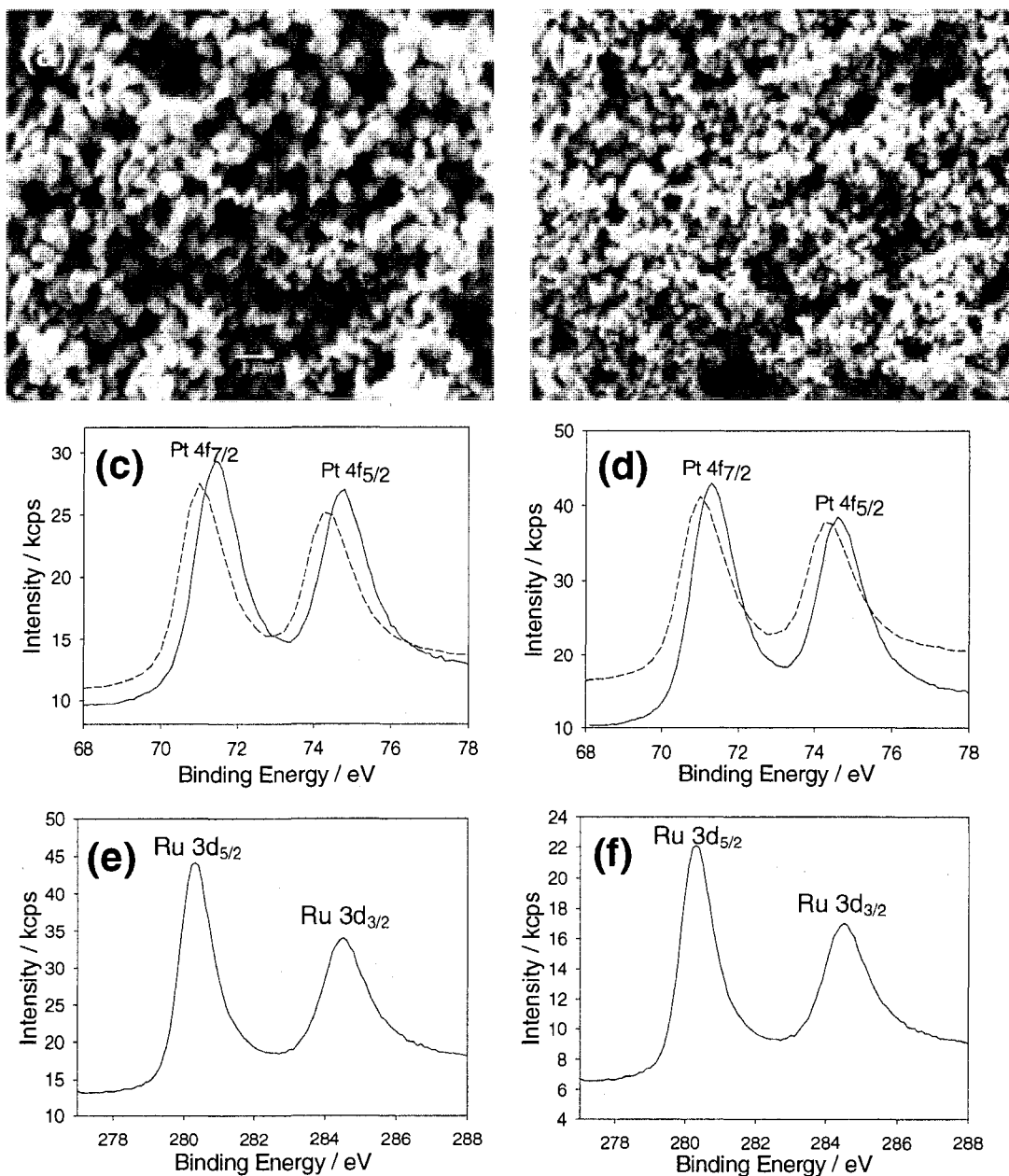
Figure 5.1. SEM images: (a) nanoporous $Pt_{60}Ru_{40}$ (S9) (b) nanoporous $Pt_{56}Ru_{29}Ir_{15}$ (S10) at 10,000x magnification. XPS spectra of the Pt 4f region for the (c) S9 and (d) S10 electrodes. (Nanoporous Pt [dashed line] is included for comparison.) In Figure 5.1c, the intensity of the nanoporous Pt indicated by the dashed line is increased by 1.5x. XPS spectra of the Ru 3d region for (e) S9 and (f) S10 electrodes.

PtRu and trimetallic PtRuIr particles with sizes 50-500 nm completely cover the titanium substrate. The prepared PtRu and PtRuIr electrodes possess nanoporous network structures. An EDS analysis was performed to determine the compositions of the samples: (a) S5, Pt; (b) S9, $Pt_{60}Ru_{40}$; and (c) S10, $Pt_{56}Ru_{29}Ir_{15}$.

XPS was used to determine whether the PtRu and PtRuIr electrodes had electronic interactions between their metallic components similar to the PtIr electrodes. In Figure 5.1c, two 4f binding peaks of Pt, identified as $4f_{7/2}$ and $4f_{5/2}$, are evident for the nanoporous Pt and PtRuIr electrodes. The Pt $4f_{7/2}$ and $4f_{5/2}$ doublets of the nanoporous Pt occur at 71.0 and 74.3 eV and at 71.3 and 74.7 eV for the nanoporous PtRuIr electrode. In Figure 5.1d, the Pt $4f_{7/2}$ and $4f_{5/2}$ doublets of the nanoporous PtRu electrode occur at 71.4 and 74.8 eV. The Ir $4f_{7/2}$ and $4f_{5/2}$ doublets for the PtRuIr electrode occurred at 60.6 and 63.6 eV versus the values for Ir metal of 60.9 and 63.9 eV [70]. With the absence of a carbon substrate, Ru was analyzed in the stronger Ru 3d region. Figures 5.1e and f show that the Ru $3d_{5/2}$ and $3d_{3/2}$ binding peaks occur at 280.2 and 284.4 eV for the PtRuIr electrode and at 280.3 and 284.5 eV for the PtRu electrode, compared to 280.0 and 284.0 eV for Ru metal [76]. The XPS results for the PtRuIr electrode reveal shifts in the Pt 4f, Ru 3d, and Ir 4f binding energies of 0.3, 0.3 and 0.2 eV, respectively. Similarly for the PtRu electrode, a shift in the Pt 4f and Ru 3d binding energies of 0.4 and 0.3 eV, respectively, was observed. Since a shift in the binding energy of core-level orbitals corresponds with a change in electron density, this indicates the presence of an electronic interaction between Pt and Ru or Ir, such as an intra-atomic charge transfer [39].

XRD analysis was used to characterize the phase and structure of the as-synthesized nanoporous electrodes. As shown in Figure 5.2a, the nanoporous Pt, PtRu and PtRuIr electrodes all display the (111), (200) and (220) reflections characteristic of the face-centred-cubic
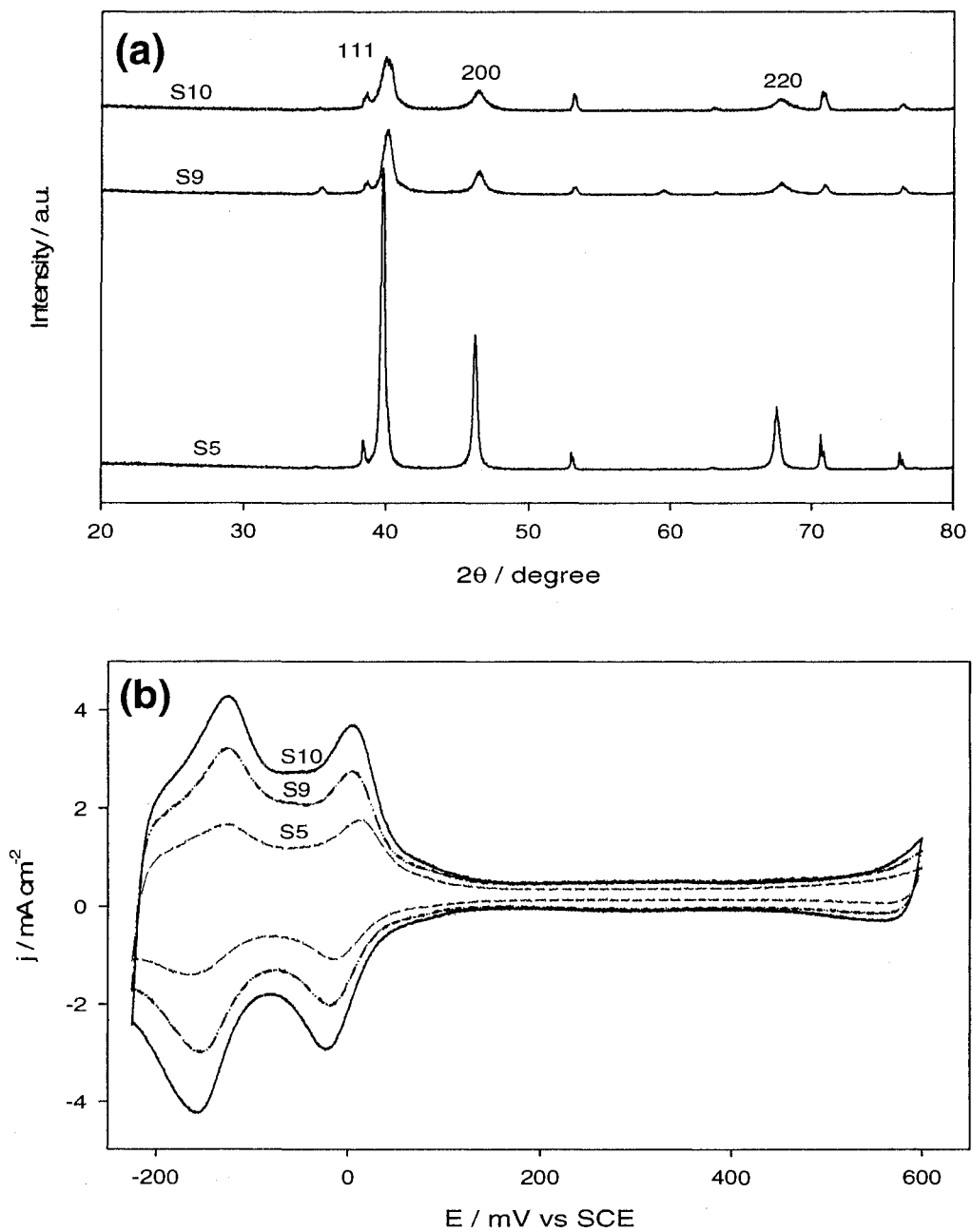
Figure 5.2. (a) XRD patterns and (b) cyclic voltammograms of the S5, S9 and S10 electrodes in

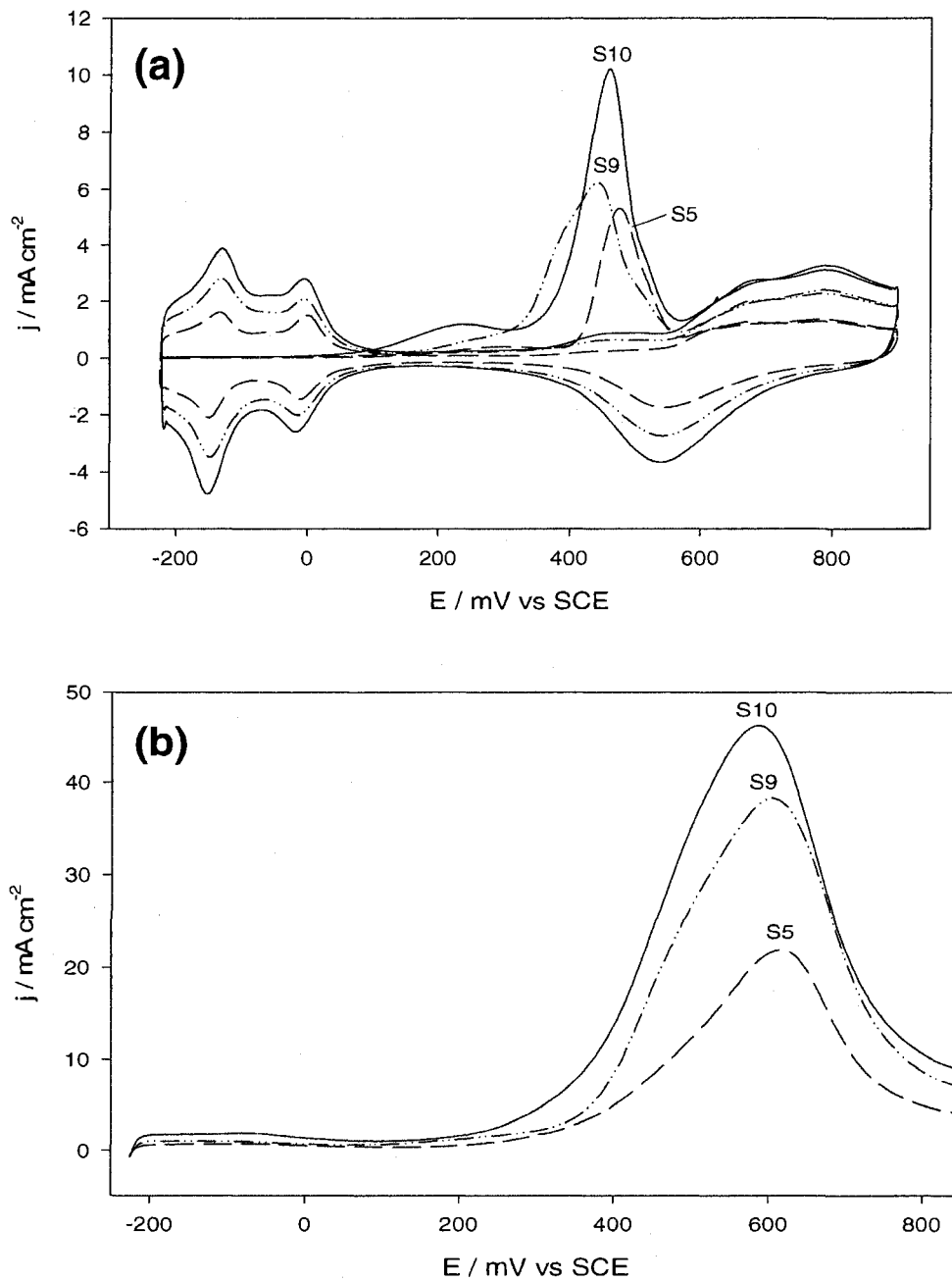0.5 M H_2SO_4 at a potential scan rate of 20 mV s^{-1}.

crystal structure. In comparison to nanoporous Pt, the PtRu and PtRuIr peaks have a positive

shift in the 2θ values, which corresponds with decreased d-spacing values and lattice constants.

Further evidence was provided by quantitative calculations of the lattice constant (a) from the

measured diffraction angles of the (220) reflection peak, which revealed a values of 0.392, 0.390

and 0.390 nm for nanoporous Pt, PtRu and PtRuIr, respectively. The peak lines for PtRu and

PtRuIr electrodes appear between the reflections of pure Pt, Ru and Ir and there are no (111),

(200) or (220) reflections which would indicate the presence of pure metals [59]. The sum of this

evidence indicates that the Pt, Ru and Ir are either fully or partially alloyed [39,67,68].

5.3 Characteristics of Hydrogen Adsorption

The cyclic voltammograms (CVs) for electrodes S5, S9 and S10 in 0.5 M H_2SO_4 at a

sweep rate of 20 mV s^{-1} are shown in Figure 5.2b. It is evident in Figure 5.2a that electrodes S5,

S9 and S10 have similar hydrogen adsorption/desorption properties: two peaks on both the

forward and reverse scans. The electroactive surface area was calculated by integrating the

intensity of the hydrogen adsorption and desorption peaks. The charges for the S5, S9 and S10

electrodes were determined to be 14.0, 24.7 and 33.8 mA cm^{-2}, respectively.

5.4 CO Oxidation on the Nanoporous PtRuIr Electrocatalysts

Carbon monoxide adsorption and oxidation were studied on the nanoporous Pt, PtRu and

PtRuIr electrodes using the procedure described in section 3.4. As seen in Figure 5.3a during the

first cycle of the CV when the potential was scanned from -225 to +100 mV, the CV curve is flat,

indicating that hydrogen adsorption is completely suppressed by the adsorbed CO. Broad CO

oxidation peaks for all the electrodes appear between +300 and +575 mV. The presence of the

hydrogen adsorption/desorption peaks and the absence of the CO oxidation peak in the second

Figure 5.3. Cyclic voltammograms of the S5, S9 and S10 electrodes (a) in 0.5 M H_2SO_4 after purging the solution with CO gas and (b) 0.5 M H_2SO_4 + 0.1 M CH_3OH at a potential scan rate of 20 mV s^{-1}.

cycle of the CVs show that the adsorbed CO was completely oxidized during the first cycle. The onset potentials of the S5, S9 and S10 electrodes for CO oxidation were +400, 175 and 100 mV, respectively. The addition of Ru significantly enhances the electrocatalytic activity of Pt towards CO oxidation, as Ru facilitates the generation of oxygen-containing species which oxidize the CO at lower potentials. Also, the presence of Ir in the S10 electrode further enhances the electrocatalytic activity of the PtRu electrode towards CO oxidation between +100 and +300 mV. An interaction between RuO_2 and IrO_2 may contribute to the Ir enhancement of the PtRu electrocatalyst. The interaction promotes the formation of hydroxyl species from water dissociation at lower potentials than occurs for PtRu electrocatalysts. Also the interaction may weaken the bond between the hydroxyl species and active catalysts sites, thereby promoting the electro-oxidation of the Co_{ads} species at lower potentials versus the PtRu electrocatalysts [77].

5.5 Electrochemical Oxidation of Methanol on Nanoporous PtRuIr Electrocatalysts

The electrochemical activity of the nanoporous PtRu and PtRuIr electrodes towards the oxidation of methanol was investigated using cyclic voltammetric and chronoamperometric methods. For clarification, only the forward scan of the CVs in 0.1 M CH_3OH + 0.5 M H_2SO_4 at 20mV s^{-1} are presented in Figure 5.3b. As shown in Figure 5.3b, the S9 electrode has a much higher peak current density and a lower onset potential for the oxidation of methanol versus the S5 electrode. This increase in the catalytic activity of Pt is consistent with previous studies conducted with similar nanoporous PtRu electrocatalysts [20]. The S10 electrode has a higher current density throughout the potential range in comparison to the S9 electrode, indicating the enhanced electrocatalytic activity of the nanoporous PtRuIr electrodes for the oxidation of methanol.
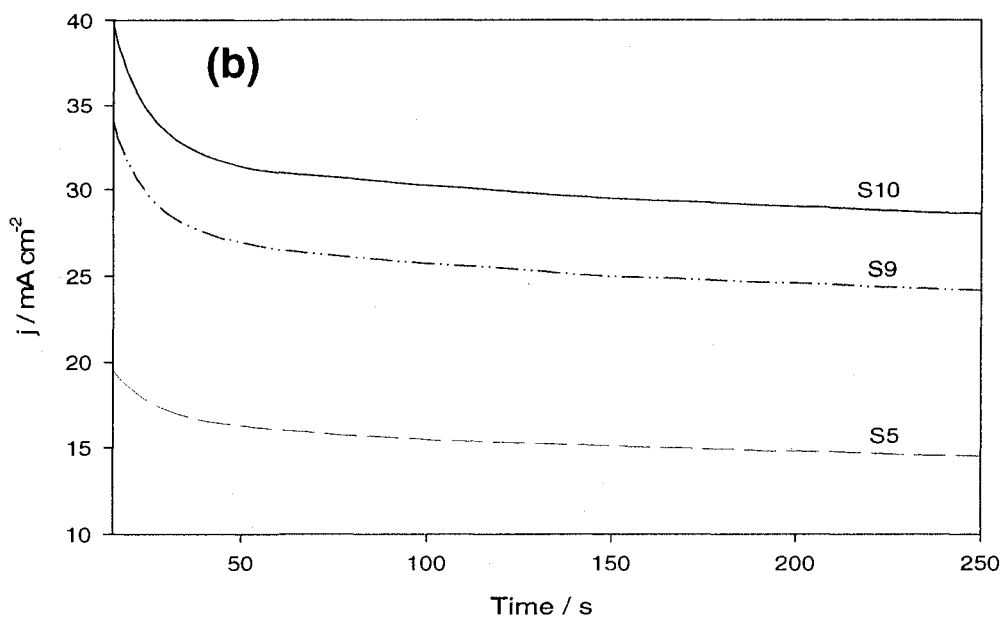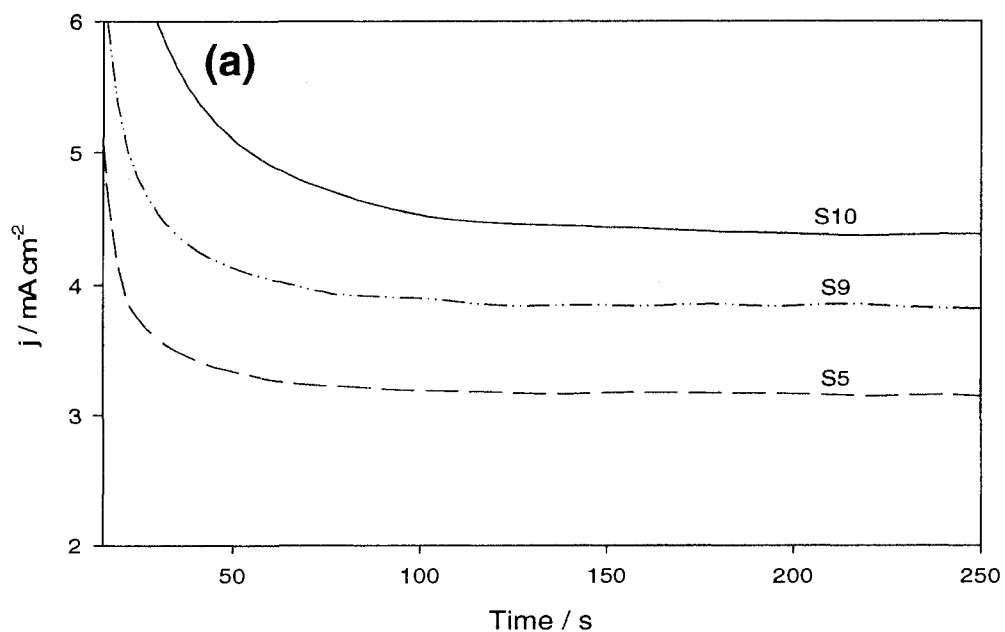
Figure 5.4. Chronoamperometry of the S5, S9 and S10 in 0.5 M H$_2$SO$_4$ + 0.1 M CH$_3$OH at potentials of (a) +300 mV and (b) +600 mV. The potential was held at 0 mV for 60 s, before being stepped to desired potential for 300 s.

Chronoamperometric experiments were used to investigate the activity of the S5, S9 and

S10 electrodes at low and high potentials. The electrode potentials were held at 0 mV for 60 s

and then stepped up to the desired potential for 300 s. Figure 5.4a shows the amperometric

responses of the S5, S9 and S10 electrodes at the potential of +300 mV. The steady-state currents

were achieved at 200 s. At 250 s the steady-state current densities of the S5, S9 and S10

electrodes were 3.2, 3.8 and 4.4 mA cm^{-2}, respectively. Therefore, it is evident that the PtRuIr

electrode is the most efficient at oxidizing methanol at lower potentials, as shown in Figure 5.4a.

The steady-state current responses at +600 mV for the S5, S9 and S10 electrodes were 14.5, 24.1

and 28.6 mA cm^{-2}, respectively, as shown in Figure 5.4b. Therefore, the presence of iridium

enhances electrocatalysis of PtRu towards methanol oxidation at low and high potentials. Similar

to the role of Ru, Ir facilitates the generation of OH_{ads} species at low potentials, thereby

enhancing the oxidation of poisonous intermediates (e.g., CO) formed during the electrochemical

oxidation of methanol [11,63].

5.6 Electrochemical Impedance Spectroscopy of Nanoporous PtRuIr Electrocatalysts

The Nyquist plots for the S5, S9 and S10 electrodes at + 300 mV in 0.1 M CH_3OH + 0.5

M H_2SO_4 are shown in Figure 5.5a. The frequency was changed from 40 kHz to 25 mHz. The

EIS results are consistent with the CV studies shown in Figure 5.3b. Figure 5.5b shows the

equivalent electric circuit used to fit the experimental data. The values for the parameters R_s, R_{ct},

CPE-T, CPE-P are listed in Table 5.1. The model can effectively fit the EIS data as the error for

the fitting is within ± 3%. S5 has the lowest CPE-T value and S10 has the highest value, which is

consistent with the electroactive surface area measurements conducted with hydrogen

adsorption/desorption. Both the S9 and S10 electrodes have much lower R_{ct} than the S5

electrode, which is consistent with the results of cyclic voltammetric and
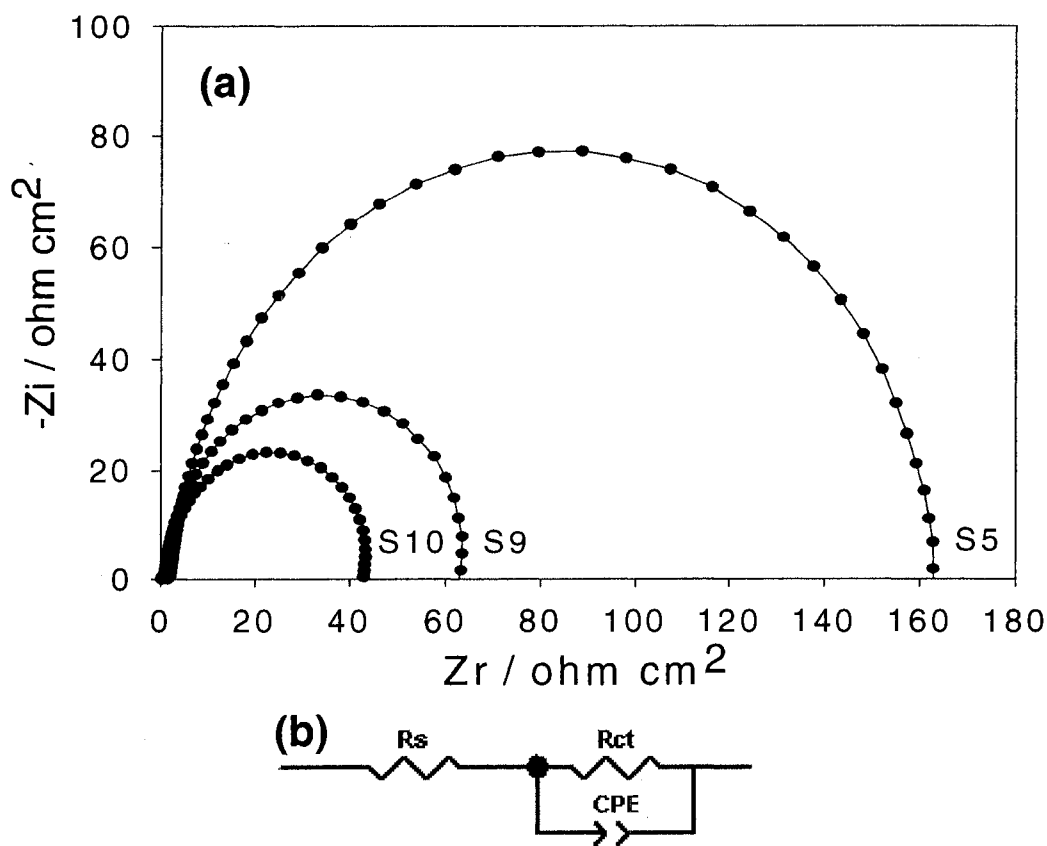
Figure 5.5. (a) Electrochemical impedance spectroscopy of the S5, S9 and S10 electrodes at a potential of +300 mV in 0.5 M H_2SO_4 + 0.1 M CH_3OH. The amplitude modulation potential was 10 mV. The frequency was changed from 40 kHz to 25 mHz. (b) The equivalent electric circuit used to fit the impedance spectra.

Table 5.1. Impedance components for S0, S1, S2, S3, and S4 at +300 mV from fitting the experimental data with the electrical circuit presented in Figure 5.5b.

	S5	S9	S10
R_s	**2.12** ± 1.05 %	**0.87** ± 2.36 %	**1.02** ± 2.20 %
R_{ct}/ Ω cm^{-2}	**162.9** ± 1.02 %	**81.41** ± 1.87 %	**45.93** ± 1.82 %
CPE-T / μF cm^{-2}	**0.0025** ± 1.02 %	**0.0057** ± 1.75 %	**0.0077** ± 1.86 %
CPE-P	**0.96** ± 0.29 %	**0.98** ± 0.54 %	**0.98** ± 0.61 %

chronoamperometric measurements shown in Figures 5.3b and 5.4. The S10 electrode shows lower R_{ct} than the S9 electrode, indicating that Ir enhances the electrocatalytic activity of the PtRu electrode towards the oxidation of methanol.

5.7 Conclusions and Future Work

Nanomaterials have a number of unique chemical and physical properties, such as high surface to volume ratios and electrocatalytic activity, which has attracted tremendous attention from researchers due to their potential for applications in a variety of areas including fuel cell and biosensor development. In this work, a number of novel Pt-based nanomaterials were prepared with the interest of studying the key electrochemical reactions in fuel cells and biosensors. These electrodes were characterized using a wide range surface characterization techniques and electrochemical methods. The major results obtained in this study are summarized below.

Nanoporous PtIr electrodes with different ratios of Pt to Ir were prepared using a one-step facile hydrothermal method. The composition and performance of the PtIr electrocatalysts was found to be dependent on the concentrations of the metal precursors, HCl and the reducing agent formaldehyde. The hydrogen adsorption/desorption experiments revealed that the synthesized nanoporous PtIr electrodes possess higher active surface areas than Pt. The electrocatalytic activity of the electrodes towards methanol oxidation and oxygen reduction was studied by CV, CA and EIS. The electrochemical studies revealed that the activity of the nanoporous $Pt_{60}Ir_{40}$ electrode towards methanol oxidation and oxygen reduction was about four times larger than that of the nanoporous Pt electrode. The high electrocatalytic activity of the nanoporous PtIr electrocatalysts shows potential for use in applications for electrochemical energy conversion. Future work could investigate the effect of the hydrothermal synthesis parameters on the

electrocatalytic activity of PtRuIr and other trimetallic Pt-based electrocatalysts.

The amperometric responses of the nanoporous PtIr electrodes towards glucose oxidation were tested in neutral media. The PtIr electrodes showed strong and sensitive current responses to glucose at a variety of potentials. Even at high concentrations of the poisoning chloride ion, the PtIr electrocatalysts produced significant responses to changes in the concentration of glucose. At a potential of +100 mV, the amperometric sensitivity of the $Pt_{62}Ir_{38}$ electrode is five times larger and much more tolerant to the presence of common interfering species than nanoporous Pt. The ease of fabrication, fast response and high sensitivity make the PtIr electrodes promising candidates for application as non-enzymatic glucose sensors. Future work could investigate the electrocatalytic activity of the PtIr electrodes with Nafion films to further reduce the interference of ascorbic acid and trimetallic PtPbIr electrodes towards glucose detection.

In summary, the electrocatalytic activities towards methanol oxidation, oxygen reduction and non-enzymatic glucose sensing have been significantly enhanced through the development of novel nanoporous PtIr nanomaterials.

References

1) Siegel, R.W. Nanophase Materials, *Encyclopedia of Applied Physics*, VCH Publishers **1994**, 11, 173.

2) Pandey, P.; Datta, M.; Malhotra, B. D. *Analytical Letters* **2008**, 41, 159.

3) Gleiter, H. *Acta Mater.* **2000**, 48, 1.

4) Murray, C.B.; Kagan, C.R.; Bawendi M.G. *Annu. Rev. Mater.* Sci. **2000**, 30, 545.

5). Masala, O.; Seshadri, R. *Annu. Rev. Mater. Res.* **2004**, 34, 41.

6) Saunders, J.R.; Benfield, D.; Moussa, W.; Amirfazli, A. *Int. J. Green Energy* **2007**, 5, 483.

7) Liu, H.; Song, C.; Zhang, L.; Zhang, J.; Wang, H.; Wilkinson, D.P. *J. Power Sources* **2006**, 155, 95.

8) Kamarudin S.K.; Daud, W.R.W.; Ho, S.L.; Hasran, U.A. *J. Power Sources* **2007**, 163, 743.

9) Liu, S-H.; Yu, W-Y.; Chen, C-H.; Lo, A-Y.; Hwang, B-J.; Chien, S-H.; Liu, S-B. *Chem. Mater.* **2008**, 20, 1622.

10) Wasmus, S.; Kuver, A. *J. Electroanal. Chem.* **1999**, 461, 14.

11) Peng, X.; Koczkur, K.; Nigro, S.; Chen A. *Chem. Commun.* **2004**, 24, 2872.

12) Chen, L.; Lu, G. *Electrochim. Acta* **2008**, 53, 4316.

13) Jingyu, S.; Jianshu, H.; Yanxia, C.; Xiaogang, Z. *Int. J. Electrochem. Sci.* **2007**, 2, 64.

14) Antolini, E.; Salgado, J.R.C.; Gonzalez, E.R.C. *Appl. Catal., B* **2006**, 63, 137.

15) Luo, J.; Maye, M.M.; Kariuki, N.N.; Wang, L.; Njoki, P.; Lin, Y.; Schadt, M.; Naslund, H.R.; Zhong, C.J. *Catal. Today* **2005**, 99, 291.

16) Deivaraj, T.C.; Chena, W.; Lee, J.Y. *J. Mater. Chem.* **2003**, 13, 2555.

17) Bock, C.; Paquet, C.; Couillard, M.; Botton, G.A.; MacDougall, B.R. *J. Am. Chem. Soc.* **2004**, 126, 8028.

18) Lin, W.F.; Iwasita, T.; Vielstich, W. *J. Phys. Chem. B* **1999**, 103, 3250.

19) Gojkovic, S.L.; Vidakovic, T.R.; Durovic, D.R. *Electrochim. Acta* **2003**, 48, 3607.

20) Peng, X.; Koczkur, K.; Chen, A. *Nanotechnol.* **2007**, 18, 561.

21) Wu, Y.M.; Li, W.S.; Lu, J.; Du, J.H.; Lu, D.S.; Fu, J.M. J. *Power Sources* **2005**, 145, 286.

22) Jayaraman, S.; Jaramillo, T.F.; Baeck, S.H.; McFarland, E.W. *J. Phys. Chem. B* **2005**, 109, 22958.

23) Yang, L.X.; Bock, C.; MacDougall, B.; Park, J. *J. Appl. Electrochem.* **2004**, 34, 427.

24) Shan, C.C.; Tsai, D.S.; Huang, Y.S.; Jian, S.H.; Cheng, C.L. *Chem. Mater.* **2007**, 19, 424.

25) Jiang, L.; Sun, G.; Sun, S.; Liu, J.; Tang, S.; Li, H.; Zhou, B.; Xin, Q. *Electrochim. Acta* **2005**, 50, 5384.

26) Colmati, F.; Antolini, E.; Gonzalez, E. R. *Electrochim. Acta* **2005**, 50, 5496.

27) Guo, Y.G.; Hu, J.S.; Zhang, H.M.; Liang, H.P.; Wan, L.J.; Bai, C.L. *Adv. Mater. (Weinheim, Ger.)* **2005**, 17, 746.

28) Hefny, M.M.; Abdel-Wanees, S. *Electrochim. Acta* **1996**, 41, 1419.

29) Zurilla, R.W.; Sen, R.K.; Yeager, E. *J. Electrochem. Soc.* **1978**, 125, 11.

30) Sljukic, B.; Banks, C.E.; Compton, R.G. *J. Iran. Chem. Soc.* **2005**, 2, 1.

31) Antione, O.; Bultel, Y.; Durand, R. *J Electroanal. Chem.* **2001**, 499, 85.

32) Kongkanand, A.; Kuwabata, S.; Girishkumar, G.; Kamat, P. *Langmuir* **2006**, 22, 2392.

33) Salgado, J.R.C.; Antolini, E.; Gonzalez, E.R. *J. Phys. Chem. B* **2004**, 108, 17767.

34) Antolini, E.; Salgado, J.R.C.; Santos, L.G.R.A.; Garcia, G.; Ticianelli, E.A.; Pastor, E.; Gonzalez, E.R. *J. Appl. Electrochem.* **2006**, 36, 355.

35) Yang, H.; Alonso-Vante, N.; Le´ger, J-M.; Lamy, C. *J. Phys. Chem. B* **2004**, 108, 1938.

36) Yang, H.; Vogel, W.; Lamy, C.; Alonso-Valente, N. *J. Phys. Chem. B* **2004**, 108, 11024.

37) Chena, G.; Delafuente, D.; SarangPani, S.; Mallouk, T.E. *Catalysis Today* **2001**, 67, 341.

38) He, T.; Kreidler, E.; Xiong, L.; Luo, B.; Zhong, C.J. *J. Electrochem. Soc.* **2006**, 153, A1637.

39) Ioroi, T.; Yasuda, K. *J. Electrochem. Soc.* **2005**, 152, A1917.

40) Wang, J. *Chem. Rev.* **2008**, 108, 814.

41) Arnold, M.A.; Small, G.W. *Anal. Chem.* **2005**, 77, 5429.

42) Lee, J.; Park, S-M. *Anal. Chim. Acta*, **2005**, 545, 27.

43) Hrapovic, S., Luong, J.H.T. *Anal. Chem.* **2003**, 75, 3308.

44) Barone, P.W.; Parker, R.S.; Strano, M.S. *Anal. Chem.* **2005**, 77, 7556.

45) Clark Jr, L.C.; Lyons, C.; *N.Y. Acad. Sci.* 1962, 102, 29.

46) Park, S.; Boo, H.; Chung, T.D. *Anal. Chim. Acta* **2006**, 556, 46.

47) Zayats, M.; Katz, E.; Willner, I. *J. Am. Chem. Soc.* **2002**, 124, 2120.

48) Ernst, S.; Heitbaum, J.; Hamann, C.H. *Ber. Bunsenges. Phys. Chem.* **1980**, 84, 50.

49) Prabhu, S.V.; Baldwin, R.P. *Anal. Chem.* **1989**, 61, 852.

50) Yuan, J.H.; Wang, K.; Xia, X. *Adv. Funct. Mater.* **2005**,15, 803.

51) Sakamoto, M.; Takamura, K. *Bioelectrochem. Bioenerg.* **1982**, 9, 571.

52) Kokkinidis, G.; Xonoglou, N. *Bioelectrochem. Bioenerg.* **1985**, 14, 375.

53) Wittstock, G.; Strubing, A.; Szargan, R.; Werner, G. *J. Electroanal. Chem.* **1998**, 444, 61.

54) X. Zhang, X.; Chan, K.-Y.; You, J.-K.; Lin, Z.-G.; Tseung, A.C.C. *J. Electroanal. Chem.* **1997**, 430, 147.

55) Wang, J.; Thomas, D.F.; Chen, A. *Anal. Chem.* **2008**, 80, 997.

56) Rodriguez, M.C.; Givas, G.A. *Electroanalysis.* **1999**, 11, 558.

57) Wang, J.; Rivas, G.; Chicharro, M. *J. Electroanal. Chem.* **1997**, 439, 55.

58) Abu Irhayem, E.; Elzanowska, H.; Jhas, A.S.; Skrzynecka, B.; Biriss V. *J. Electroanal. Chem.* **2002**, 538, 153.

59) Wang, J.; Holt-Hindle, P.; MacDonald, D.; Thomas, D.F.; Chen. A. *Electrochim. Acta* **2008**, In Press.

60) Peng, X.; Koczkur, K.; Chen, A. *J. Phys. D: Appl. Phys.* **2008,** 41, 095409.

61) Holt-Hindle, P.; Yi, Q.; Wu, G.; Koczkur, K.; Chen, A. *J. Electrochem. Soc.* **2008**, 155, K5.

62) Schmidt, T.J.; Gasteiger, H.A.; Stab, G.D.; Urban, P.M.; Kolb, D.M.; Beh, R.J. *J. Electrochem. Soc.* **1998**, 145, 2354.

63) Chen, A.; La Russa, D.J.; Miller, B. *Langmuir* **2004**, 20, 9695.

64) Adžić, R. in *Electrocatalysis,* Lipkowski, J., Ross, P.N., Wiley: New York, NY, **1998**, 197.

65) Toda, T.; Igarashi, H.; Uchida, H.; Watanabe, M. *J. Electrochem. Soc.* **1999**, 146, 3750.

66) Ma, L.; Sui, S.; Zhai. Y. *J. Power Sources* **2008**, 177, 470.

67) Gasteiger, H.A.; Markovic, N.; Ross Jr, P.N.; Cairns, E.J. *J. Phys. Chem.* **1993**, 97, 12020.

68) Arico, A.S.; Antonucci, P.L.; Modica, E.; Bagilo, V.; Kim, H.; Antonucci, V. *Electrochim. Acta* **2002**, 47, 3723.

69) Blasini, D.R.; Rochefort, D.; Fachini, E.; Alden, L.R.; DiSalvo, F.J.; Cabera, C.R.; Abruna, H.D.; *Surf. Sci.* **2006**, 600, 2670.

70) Wagner, C.D.; Riggs, W.M.; Davis, L.E.; Moulder, J.F.; Muilenberg, G.E. *Handbook of X-ray Photoelectron Spectroscopy*, Perkin-Elmer Co: Eden Prairie, MN, **1979**.

71) Sano, M.; Kamino, A.; Okamura, J.; Shinkai, S. *Langmuir.* **2001**, 17, 5125.

72) Liao, S.; Holmes, K-A.; Tsaprillis, H.; Birss, V. *J. Amer. Chem. Soc.* **2006**, 128, 3504.

73) Beden, B.; Largeaud, F.; Kokoh, K.B.; Lamy, C. *Electrochim. Acta.* **1996**, 41, 701.

74) Bae, I. T.; Yeager, E.; Xing, X.; Liu, C. C. *J. Electroanal. Chem.* **1991**, 309, 131.

75) Yuan, J.; Wang, K.; Xia, X.; *Adv. Funct.* Mater. **2005**, 5, 803.

76) Aric, A. S.; Creti, P.; Kim, H.; Mantegna, R.; Giordano, N.; Antonucci. V. *J. Electrochem. Soc.* **1996**, 143, 3950

77) Liang, Y.; Zhang, H.; Zhong, H.; Zhu, X.; Tian, Z.; Dongyan, X.; Yi, B. *J. Catal.* **2006**, 238, 468.

78) Koczkur, K.; Yi, Q.; Chen, A. *Adv.Mater.* **2007**, 19, 2648.